A Stepwise Reaction Achieves Ultra-Small Ag_2ZnSnS_4 Nanocrystals

Francisco Yarur Villanueva,[1] Minhal Hasham,[1¶] Philippe B. Green,[1#] Christian J. Imperiale,[1†] Samihat Rahman,[1] Darcy C. Burns,[1] Mark W.B. Wilson[1*]

[1]Department of Chemistry, University of Toronto, Toronto, ON, M5S 3H6, Canada

¶ Present address: Department of Chemistry, Gordon Center for Integrative Sciences, University of Chicago, Chicago, IL 60637, USA.

[#]Present address: Department of Chemistry, École Polytechnique Fédérale de Lausanne, Sion, CH A3 398, Switzerland

[†]Present address: Polytechnique Montréal, Department of Engineering Physics, Montréal, QC, Canada, H3T 1J4

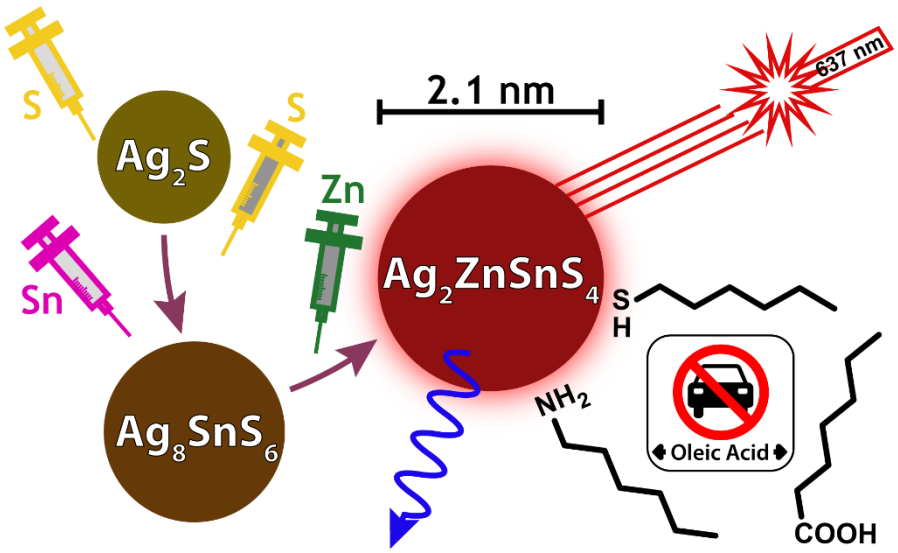

Abstract

Pirquitasite Ag_2ZnSnS_4 (AZTS) nanocrystals (NCs) are emergent, lead-free emissive materials in the coinage chalcogenide family with applications in optoelectronic technologies. Like many multinary nanomaterials, their phase-pure synthesis is complicated by the generation of *e.g.* binary/ternary chalcogenide and metallic impurities. Here, we develop a stepwise synthetic procedure that controls the size, morphology, and transformations of acanthite-like (Ag_2S) and canfieldite-like (Ag_8SnS_6) intermediates. This reaction scheme grants the production of small AZTS NCs (diameter: 2.1–4.0 nm) that have not been achieved through established single-injection procedures—expanding the accessible range of quantum-confined AZTS emission to shorter wavelengths (λ: 650–740 nm). We show that the initial sulfur stoichiometry is the key handle for template-size tunability and reveal that temporally separating transformation steps is crucial to obtaining phase-pure AZTS NCs with emission λ<740 nm. We then use NMR and optical spectroscopies to demonstrate that the installation of thiol ligands improves colloidal stability, while exposure to carboxylic acids does not. Finally, facilitated by this enhanced synthetic control, we show that our ultra-small AZTS NCs can act as effective, less-toxic sensitizers for red-to-blue triplet fusion upconversion. Our results highlight transferrable insights for the synthesis and post-synthetic treatment of complex less-toxic quaternary nanocrystalline systems.

Key words: pirquitasite, AZTS, kesterite, nanocrystals, quantum dots, colloidal synthesis, NMR, surface chemistry, photophysics, triplet fusion upconversion

Introduction

The current synthetic control and the understanding of the photophysics of nanocrystals (NCs) has enabled their use in myriad applications including bioimaging, light-emitting devices, and sensing.[1-4] Many reports have featured established binary (PbS, CdS/Se, In/GaAs) and, more recently, ternary ($CuInS_2$, halide perovskite) NCs.[5] However, these heavily studied systems involve chemical elements where sustainability is a concern, due to questions regarding toxicity or terrestrial abundance.[5-6] Consequently, there is a desire to develop new and environmentally friendly alternatives.

For example, quaternary kesterite-Cu_2ZnSnS_4 (k-CZTS) NCs have been extensively explored as candidate material for photovoltaic and photocatalytic applications due to the earth-abundance and low toxicity of the constituent atoms.[7] Unfortunately, k-CZTS can be challenging to employ in optoelectronic applications because of a susceptibility to anti-site defects that trap carriers and suppress photoluminescence. These defects form when Cu and Zn switch positions in the lattice, which occurs with a low energy barrier due to their similar ionic radii.[8-10] To overcome these drawbacks, NCs composed of the underexplored quaternary silver analog Ag_2ZnSnS_4 (AZTS) have been recently investigated because of its decreased predisposition to anti-site defects.[11] Initial reports have confirmed their visible absorption with bulk bandgap value of 1.50 eV,[11-12] tunable up to 1.68 eV *via* size-controlled synthesis that exploits quantum confinement. AZTS NCs display emission in the red/near-infrared that can be improved through the growth of a ZnS shell, and tuned between 740–850 nm.[13] This red/near-infrared wavelength range is of particular interest for applications such as thin-film optoelectronics and NC-sensitized triplet-fusion upconversion, where Pb-based NCs have been dominant.[1, 3, 14-18] Thus, AZTS NCs stand as an intriguing candidate for a new generation of less-toxic optoelectronic devices.

Reported synthetic procedures for AZTS NCs vary considerably. For example, current syntheses make use of various temperatures (140–240 ºC), different solvents [octadecene,[11] oleylamine (OLA),[19-20] oleic acid (OA)[11]], and a number of tin sources [Sn(II) *vs.* Sn(IV)],[11, 19, 21] each with differing reactivities. The properties and emissivity of AZTS NCs from these various reactions range widely, but the diversity of precursors and solvents blurs a general understanding of the formation mechanism. Such mechanistic understanding is paramount for the controlled growth of high-quality multinary NCs where the larger combinatorial space can allow the formation of undesired phases.[22-24] For instance, metallic (*e.g.* Ag^0), binary (Ag_2S, SnS, SnS_2, ZnS) and ternary (Ag_8SnS_6, Ag_2SnS_3) phases could plausibly form during reactions targeting AZTS NCs. Such species can both serve as synthetic intermediates—regulating/complicating the reaction kinetics—as well as unwelcome impurities in the intended AZTS product. Therefore, it is important to attain a unified understanding of the effects of solvents, precursors, and intermediate phases to control and direct the formation of phase-pure AZTS NCs.

We recently demonstrated that the synthesis of quaternary CZTS NC polymorphs can be guided by the intentional formation of selected, binary $Cu_{2-x}S$ templates[24]—in essence achieving a cleaner reaction pathway through a complex material family by removing degrees of synthetic freedom. An advantage to the controlled generation of intermediates is the separation of conversion steps in time, which can prevent the unintended generation of undesired phases. Further, conversion mechanisms that preserve the size of the parent/templating NC can expand the accessible range of sizes/shapes beyond those easily obtainable directly through a heat-up or hot-injection route.[25-26] However, the existence and relevance of intermediates in the synthesis of AZTS is not yet clear,

even though some binary/ternary phases have been reported as impurities in the final product.[20] Particularly, Ag_2S intermediates have not yet been identified, though Ag_2S impurities have been detected in the mechanochemical synthesis of Ag_2FeGeS_4,[27] a similar crystalline system. These observations raise the possibility to implementing a template-guided synthesis of AZTS NCs, particularly considering the well-established cation exchange procedures in the analogous, copper-based CZTS system.[24, 28-29]

In addition to the advantages provided through synthetic control by templated reactions, post-synthetic processing is essential to the use of NCs in many optoelectronic technologies because many photophysical properties are strongly correlated to the surface chemistry.[30-32] Then, the development of strategies for post-synthetic modification is aided by an understanding of ligand binding motifs through which ligands interact with the surface of NCs. However, experimental explorations of the surface chemistry of AZTS NCs have not been reported. Indeed, this surface is expected to be complex. For instance, we and others have shown that the binding motifs of simpler binary NCs are already heterogeneous.[33-37] In addition, the Hens group has reported that the surface chemistry of ternary nanocrystals of In(As,P)[38] and $CuInS_2$[39] show increased complexity that depends on multiple parameters (*e.g.* stoichiometry, shape, and local variation in binding/ligation at facet-edges and apices). Quaternary NC systems bring further complications as every additional metal element combinatorically expands the accessible multi-metallic co-ordination environments. Thus, the surface chemistry of AZTS NCs is expected to be rich, so improved understanding can guide the development of tailored ligand exchange reactions to support their implementation in technologies. Here, nuclear magnetic resonance (NMR) spectroscopy is particularly useful to probe the surface chemistry of NCs.[40] To aid the interpretation of our experimental results, we briefly summarize the key techniques that we employ in Supplementary Section 1, and refer the interested reader to established texts for comprehensive discussion.[40-44]

Then, knowledge of the nanocrystal surface is particularly useful to improve the performance of technologies that rely on tailored functionalization. For instance, triplet-fusion upconversion is an approach to generate high-energy photons from longer-wavelength light.[45] It is based on the coalescence of two spin-triplet molecular excitons to create one higher-energy singlet, which can then fluoresce. Effective performance at modest excitation intensities is possible because molecular triplets can be very long-lived (>>μs), allowing a large concentration of triplets to build up, so that bimolecular fusion outcompetes monomolecular triplet decay. Triplet-fusion upconversion is of interest for applications including bioimaging and *in situ* photochemistry, exploiting the superior penetration of *e.g.* biological tissue by longer-wavelength light.[1, 3, 46-49] However, because direct triplet photoexcitation is spin-forbidden in relevant molecular systems, leading upconversion systems use external sensitizers that can efficiently generate triplet states.[50] NCs can be used as triplet-sensitizers,[3, 51-52] taking advantage of their large molar absorption coefficients, spin-mixed band-edge states, and functionalizable surfaces.[53] Leading strategies further improve upconversion performance *via* the extraction of photoexcitations from the NC to surface-anchored ligands.[54] Examples of such upconversion systems employ PbSe,[51] PbS,[3, 55] CdSe,[52] $CuInS_2$ NCs,[56] and $CuInSe_2$,[57] each of which contains chemical elements that are either toxic or poorly abundant. Thus, more-sustainable alternatives could advance the implementation of NC-sensitized triplet fusion upconversion technologies.

Here, we report a synthetic approach that yields Ag_2ZnSnS_4 NCs with improved control of size, morphology, and phase purity. Supported by our mechanistic investigations, we designed a

synthetic procedure that controllably forms the key reaction intermediates *in situ* in a stepwise fashion, passing through acanthite-like (Ag_2S) and canfieldite-like (Ag_6SnS_8) phases that template the ultimate, phase-pure, pirquitasite (Ag_2ZnSnS_4) product. Vitally, our stepwise synthetic route ensures sulfur-poor conditions during the formation of the Ag_2S intermediate, favouring the morphology that is then a superior template for AZTS NCs. We perform this reaction in OLA to access improved colloidal stability, so the purity of the AZTS product is also aided by rapid heating and a low reaction temperature (<80 ºC) to avoid the unwanted reduction of the silver precursor. We substantiate this approach and confirm the identity of key intermediates by mapping the stepwise evolution of the reaction using X-ray diffraction, Raman measurements, elemental analysis, optical spectroscopy, and electron microscopy. Taken together, our experiments reveal that separating the conversion steps in time is crucial to obtaining small AZTS NCs with emission < 740 nm.

We then gain insight into the surface chemistry of AZTS nanoparticles and are able to modify their surface to improve their photophysical performance. We use spectroscopy to demonstrate that thiols are an effective post-synthetic additive that can enhance both the colloidal stability and the optical properties of AZTS NCs by displacing native OLA ligands in an L-for-L exchange. Conversely, through 1D and 2D ^{1}H NMR, we show that the introduction of carboxylic acids indirectly pulls dynamically bound OLA ligands from the surface of the NCs, inducing significant aggregation. Finally, in a demonstration of the of the latent value of these less-toxic/earth-abundant AZTS NCs that is unlocked by this significantly improved size control and colloidal/photophysical quality, we demonstrate that AZTS from our modified synthesis can act as sensitizers for red-to-blue triplet-fusion upconversion.

Results/Discussion

Synthesis in OLA is advantageous, but it is vital to control pre-injection Ag^0 NP formation to achieve phase-pure AZTS NCs

With the overall goal of understanding the formation of AZTS NCs and synthesizing phase-pure, emissive, and small particles, we first focused on the choice of solvent/ligands. Syntheses have been reported in both OA[11] and OLA,[19-20] and we performed test reactions following both reported procedures (See Methods). In our hands, we observed that AZTS NC reactions in OA yield non-emissive products that aggregated after washing with acetone, and were not readily redispersible in nonpolar solvents (Figure S1). By contrast, comparable syntheses in OLA yielded NCs that remained stable in solution following washes and exhibited notably brighter emission near λ: 750 nm, consistent with AZTS NCs (Figure S2). Though these latter qualities are already attractive, this emission was very broad and exhibited a pronounced shoulder extending into the infrared, consistent with *e.g.* significant size-dispersity or the presence of impurity NCs. Further, amine solvents are known to reduce metallic precursors at elevated temperatures, which can result in the generation of metallic nanoparticles.[24, 58] Indeed, we previously showed that the comparable pre-formation of metallic Cu NPs interfered with the colloidal synthesis of related CZTS NCs, particularly giving rise to a wide range of particle sizes and morphologies.[24] Consequently, we hypothesized that similar issues were arising in the synthesis of AZTS NCs in OLA at elevated temperatures (*e.g.* 140-250 °C,[11, 19-20]), and sought strategies to mitigate the reduction of Ag to regularize the reaction and thereby unlock the other apparent advantages of this solvent/ligand.

To explore this hypothesis, we first studied the interaction between the silver acetate precursor and OLA in isolation (SI Section 1, Figure S3), and used UV-Vis, PXRD, and TEM to confirm that large, size-disperse Ag^0 form within minutes >80 °C—*i.e.* the conditions previously used to synthesize AZTS NCs.[19-20] This finding aligns with previous demonstrations of the production of metallic silver NPs in reducing conditions.[59-61]Accordingly, we then investigated the implications of the presence of Ag NPs in the subsequent formation of AZTS NCs. Specifically, we performed a pair of AZTS syntheses at 80 °C and 100 °C, using a single injection of all remaining precursors into silver acetate in OLA (See Methods). At the higher temperature, the formation of Ag NPs prior to injection was heralded by a prominent yellow colour, matching the behaviours observed in the previous focused experiments (Figure S3). Then, following injection of the remaining precursors, the solution immediately turns black, but we do not observe appreciable photoluminescence until 45 minutes have passed (Figure 1a). We first detect emission peaked at λ: 705 nm. This PL is consistent with AZTS NCs, [11] and we will subsequently confirm that such reactions yield this product (Figures S4, S5, Table S1, and S6). However, in this reaction, the very feint emission at this stage is consistent with non-emissive particles or a low synthetic yield. Still, the PL peak is at a shorter wavelength relative to previous reports, which heralds the ability of lower-temperature reactions in OLA to generate smaller AZTS NCs. From this point, the PL strengthens and progressively re-shifts as the AZTS particles form and grow (Figure 1a), until reaching a peak brightness four hours after injection. Unfortunately, we observe a broad PL linewidth at this time (Full-width at half-max: $FWHM_{100°C} = 245$ meV). This is consistent with a size-disperse ensemble, and TEM images taken of the products at 90 minutes already show

pronounced variation in particle size and imaging contrast, implying poor synthetic purity (Figure 1a).

Strikingly, the comparable synthesis of AZTS NCs in OLA run at 80 °C (where the formation of Ag NPs is disfavoured) exhibits a qualitatively different reaction trajectory. First, and counterintuitively, this lower-temperature reaction proceeds more-rapidly. The synthesis again yields emissive AZTS particles, indicated by the prominent, characteristic[62] modes at 345 cm^{-1} and 365 cm^{-1} in Raman spectra (Figure S5a) and a contribution to the overall PL emission that is

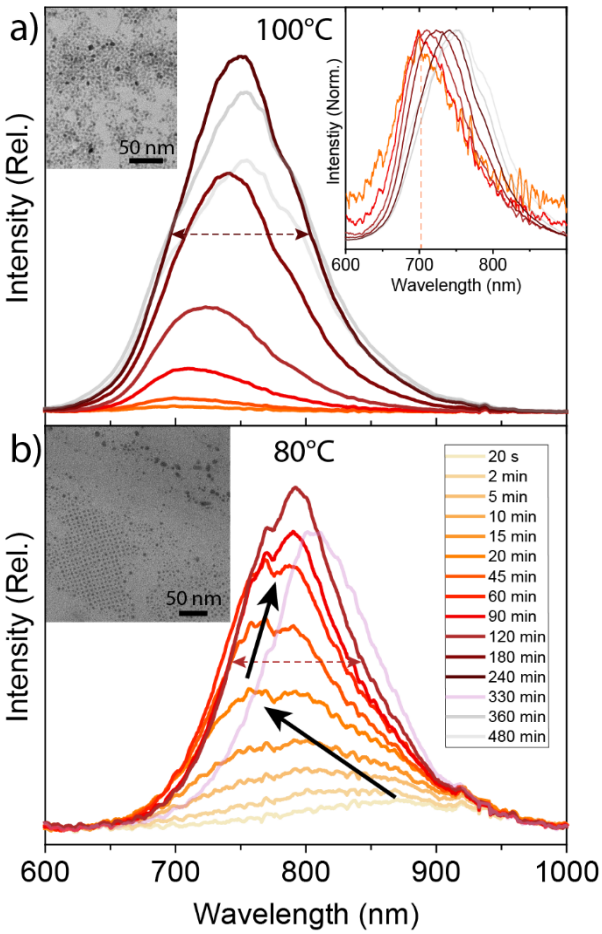

Figure 1. Pre-injection reduction of the silver precursor impacts the subsequent formation of AZTS NCs.
a,b) Photoluminescence (PL) spectra from aliquots tracking the growth of AZTS NCs synthesized *via* the conventional single sulfur injection at a) 100 °C and b) 80 °C. At 100 °C, there is significant pre-injection formation of Ag NPs (Figure S3), and we do not observe PL until the 45 min aliquot. The first, feint emission peak is detected at λ: 705 nm (see inset). This PL is consistent with AZTS NCs (Figure S4, S5), but is at shorter wavelengths compared to previous reports, implying the presence of smaller AZTS particles (in a low yield.) However, by the time this emission is appreciable (*e.g.* the 90-minute aliquot) the PL linewidth is broad, and TEM (inset) indicates poor purity and large size-dispersity. b) At 80 °C, where the formation of Ag NPs is diminished (Figure S3), the earliest aliquots (20 s) show a broad peak at λ: 870 nm, indicating that α-Ag_2S intermediates are already present. This feature becomes a shoulder to a strengthening main peak (first centered at λ: 760 nm at 15 minutes, before red-shifting), which reflects the emission from AZTS NCs as they form and then grow. Counterintuitively, the overall formation of emissive AZTS NC is faster in the lower-temperature reaction, where the (larger) final products have narrower emission linewidths and better size dispersity relative to (a) (*e.g.* inset TEM from the 60-minute aliquot). However, AZTS NCs smaller than previously reported are not observed under these conditions, and prominent impurities remain.

already observable 10 minutes after injection as a shoulder near λ: 760 nm (Figure 1b). Notably, peak brightness is reached in two hours at 80 °C rather than four hours required at 100 °C. Then, the lower-temperature reaction shows encouraging signs of improved synthetic quality. For example, a narrower emission linewidth at max-brightness ($FWHM_{80°C}$ = 214 meV), and evidence of a self-organization into an ordered NC superlattice in TEM (Figure 1b).

To show the contrasting effects of the two reaction temperatures in the sharpest relief, we designed a 'toy' AZTS reaction that would purposefully enhance the formation of Ag NPs prior to sulfur injection, but otherwise match our optimized synthesis (*vide infra*). This was inspired by the demonstration by Ning and Zou that Ag NPs promote the formation of Ag_8SnS_6/Ag_2S heterostructures.[63] Specifically, we brought a solution of Ag(OAc) in OLA to 100 °C and held it at this temperature for 3 minutes, before reducing the temperature to 80 °C and injecting the remaining precursors needed to synthesize AZTS in a step-wise sequence (Methods). This pre-injection heating caused a pronounced colour change, consistent with reduced silver, and TEM images of aliquots taken at this time show large (~15 nm) nanoparticles (Figure S3b). Following injection, further aliquots were taken periodically (Figure S4c,d), but we focus on the early reaction stages where the smallest AZTS could be obtained (Figure S4c, Figure 1a). In the 10s aliquot from the toy reaction we observe: small NCs *via* TEM (Figure S4b), the characteristic modes of AZTS in the Raman spectra (Figure S4a), and the PL emission spectrum expected for very small AZTS particles (Figure S4c). This is considerable evidence that AZTS NCs can be produced from solutions that include Ag NPs. However, we also observe Raman peaks at 309 cm^{-1} and 91 cm^{-1} that are absent in the control reaction (Figure S4a). These are characteristic modes of Ag_8SnS_6[64] and α-Ag_2S,[65] respectively. Thus, these peaks indicate the presence of the corresponding impurities in the toy reaction at this time, and link the pre-injection presence of Ag NPs to the partial subsequent conversion to the desired AZTS product. Further, TEM images of the 10s aliquot from the toy reaction show gross morphological heterogeneity, including the presence of much larger (>20 nm), high-contrast nanostructures (Figure S4b). Therefore, we concluded that syntheses of AZTS NCs in OLA should be run at initial temperatures no greater than 80 °C to minimize the (pre-injection) formation of Ag NPs, because these NPs alter the reaction kinetics and hinder the production of phase-pure quaternary product.

However, returning to the single-injection reaction run at 80 °C (Figure 1b), it is also evident that the lower temperature alone is not enough to afford small, phase-pure AZTS NCs. For instance, larger impurities are visible in the TEM image and indicate the presence of α-Ag_2S nanoplatelets throughout the reaction (Figure 1b (inset), S5b,c). Moreover, we do not observe short-wavelength emission at the early stages of the reaction at 80 °C, implying that small AZTS NCs are not effectively generated. Indeed, though we observe PL from the first aliquot (taken at 20 s), it exhibits a broad peak centered at λ: 870 nm that we assign to the emission of nanostructured α-Ag_2S.[66] This differs sharply from the same reaction run at 100 °C, from which we do not detect PL for 45 minutes. Instead, at 80 °C, the PL from the α-Ag_2S is slowly depleted as the characteristic emission from AZTS rises, implying that the binary species is serving as a reaction intermediate, while also persisting as a terminal impurity in this synthesis (Figure S7). Consequently, we aimed to better manage the formation and subsequent transformation of Ag_2S species to realize the potential of this synthesis to afford small, phase-pure AZTS NCs.

Sulfur stoichiometry modulates Ag_2S template morphology, which impacts AZTS phase-purity

Continuing our efforts to design a synthesis of ultra-small AZTS with high phase purity, we next explored the influence of sulfur stoichiometry on the formation and nature of Ag_2S intermediate species. We drew insight from previous studies of related materials with anisotropic intermediates and a final cation-exchange step,[24, 67-69] where it was shown that uneven diffusion of cations from reactions that proceed from a facet or edge can lead to incomplete, morphology-dependent exchange. A particularly relevant example in the silver chalcogenide family is the formation of Ag_8SnSe_6 crystals, where large Ag_2Se nanostructures have been observed to prevent the full incorporation of Sn^{4+}.[70] Analogous Ag_2S nanostructures have been identified in the synthesis of Ag_2S particles,[71-72] and these intermediates have a platelet-like appearance in TEM. Thus, in the synthesis of AZTS, we suspected that the formation of large, anisotropic α-Ag_2S nanostructures (*e.g.* nanoplatelets) could lead to an inhomogeneous conversion upon Sn^{4+} and Zn^{2+} injection, and hypothesized that their suppression could improve the synthetic quality of the final multinary product. Notably, the stoichiometric precursor ratios for the overall synthesis of AZTS are very sulfur-rich with respect to the initial formation of binary Ag_2S particles. These conditions enhance nanoplatelet formation in the targeted synthesis Ag_2S nanoparticles,[72] so we expected that single-injection syntheses of AZTS would be similarly prone to form these larger intermediates.

To test this hypothesis, we synthesized α-Ag_2S nanoplatelets *in situ* using sulfur-rich conditions (1:2 Ag:S, stoichiometric ratio in the Ag_2ZnSnS_4 system) and contrasted this with a reaction with 1:0.41 Ag:S designed to generate a sulfur-poor environment in the initial nucleation period. To gain insight into the dynamic reaction conditions and evaluate the size and morphology of prompt α-Ag_2S intermediates, we used a syringe pre-filled with cold EtOH to withdraw an aliquot from each reaction immediately following TMS-S injection (See Methods). These aliquots were dispensed into a vial, centrifuged, and the pellet was re-dispersed in toluene for TEM and PXRD analysis. TEM images from the sulfur-rich synthesis show large, irregular nanoplatelets (20-100 nm, Figure 2a), while the PXRD diffractogram displays sharp reflections that closely resemble the reference pattern for α-Ag_2S (Figure S8a). Thus, we concluded that the traditional reaction stoichiometry for AZTS forms large α-Ag_2S nanoplatelets *in situ* at 80 °C. In sharp contrast, comparable TEM imaging of the sulfur-poor reaction (Figure 2d) did not detect large α-Ag_2S nanoplatelets, suggesting that their formation had been effectively restrained. Instead, we observed the formation of smaller, well-separated, spherical nanoparticles with a well-defined average size of 3.4 ± 0.6 nm (Figure 2d). PXRD on these samples reveals broad reflections (Figure S8a) that match previous reports for small Ag_2S nanoparticles.[71, 73] The strongly-broadened form has previously been ascribed to an amorphous phase, though the diffractogram does not rule out an acanthite-like structure (*e.g.* distorted α-Ag_2S) given the small particle size. As discussed above, we expect that small nanoparticles would be superior templates (relative to large nanoplatelets) for the formation of phase-pure ultra-small AZTS NCs, so we continued to compare these strategies.

Specifically, to assess the effect of α-Ag_2S nanoplatelets on the overall synthesis of AZTS, we carried on with the two syntheses described above (sulfur-rich and -poor) by injecting the Sn^{4+} and Zn^{2+} precursors. We monitored the progress of the reactions by taking further aliquots (See Methods). These mixtures were emissive, so optical spectroscopy gave immediate insight (Figure

S8b). Upon the injection of the Sn and Zn sources into the sulfur-rich reaction, we noticed a broad emission feature in the 700-900 nm range that evolved over the course of the reaction (Figure S8b). Emission from both AZTS and α-Ag_2S nanoplatelets has been reported in this general range.[11, 73] This differed from our observations in the sulfur-poor reaction (Figure 3d), where the emission was narrower, with a clear peak that evolved from 650 to 790 nm as the reaction progressed. TEM images of the products of the initially sulfur-poor synthesis show consistent, spherical particles (Figure 2e, diameter = 3.2 ± 0.4), and elemental analyses performed on comparable sulfur-poor syntheses are consistent with the expected quaternary stoichiometry for AZTS (*vide infra*). By contrast, the sulfur-rich reaction yields a range of structures (*i.e.* spherical particles with surrounding residues and larger irregular structures, Figure 2b, S9), which is consistent with the presence and partial conversion of α-Ag_2S nanoplatelets. Raman measurements from either synthesis (Figure 2c,f) confirm the formation of some AZTS *via* the features at 365 cm^{-1} and 345 cm^{-1}, for instance because the latter (dominant) signal can be assigned to the A_1 mode stemming from the symmetric motion of S atoms in AZTS.[62] However, the Raman spectra from the sulfur-rich synthesis (where α-Ag_2S nanoplatelets are prominent in TEM) show additional features that correspond to binary/ternary impurities. For instance, we recognize a prominent mode at 93 cm^{-1} in the sulfur-rich reaction that corresponds to bulk α-Ag_2S.[65] This implies slowed conversion to the quaternary AZTS phase, consistent with our hypothesis that large nanoplatelets hinder cation diffusion and inconveniently provoke an anisotropic conversion. Further, even 30 minutes into the sulfur-rich reaction, we observe modes at 230, 265, and ~309 cm^{-1} that are associated with bulk ternary canfieldite,[64] indicating that Zn incorporation is hindered, and that persistent ATS impurities form when α-Ag_2S nanoplatelets are present. Taken together, our observations link the presence of large α-Ag_2S nanoplatelets during the initial nucleation of binary templates with poor subsequent phase-purity of the desired AZTS product.

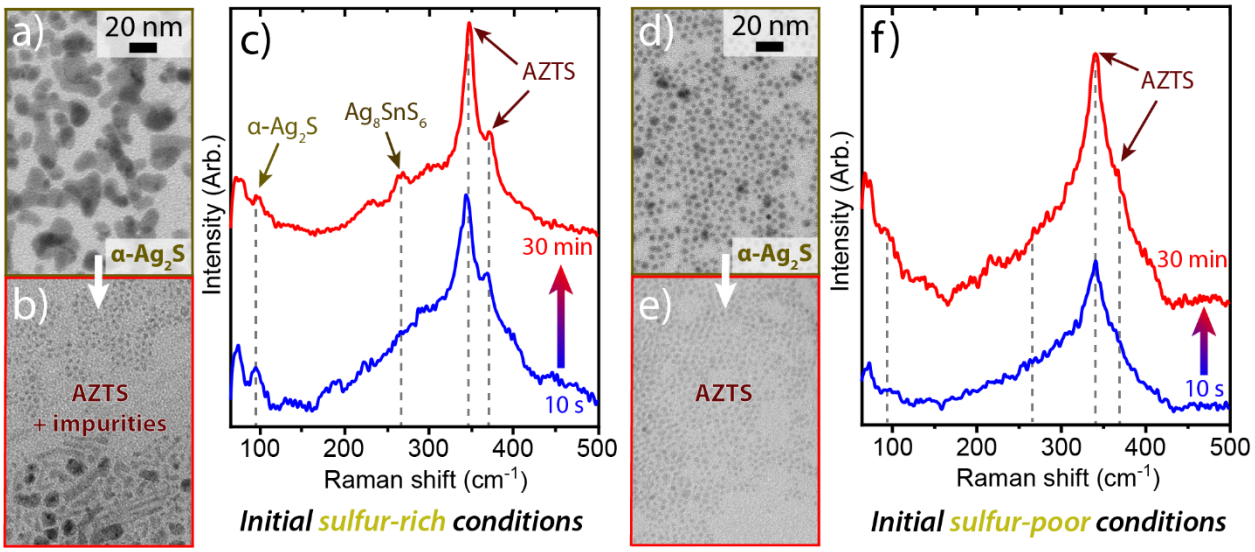

Figure 2. Sulfur availability influences the morphology of binary Ag_2S intermediates and the phase-purity of subsequent Ag_2ZnSnS_4 nanocrystals.

a,d) TEM images from aliquots extracted immediately upon sulfur injection (0s) from *two-component* reactions run at a) sulfur-rich (Ag:S 1:2) and c) sulfur-poor (Ag:S 1:0.41) conditions. Though work-ups are identical, we observe large α-Ag_2S nanoplatelets only with excess sulfur.

b,e) TEM images from aliquots extracted 30 minutes after injection from *four-component* reactions to form Ag_2ZnSnS_4 nanocrystals. In b), all sulfur precursors are present initially, causing sulfur-rich conditions for the initial formation of Ag_2S nanoparticles. In e) , sulfur addition is staggered to achieve sulfur-poor conditions at the reaction outset. Four-component reactions that are initially sulfur-rich (b) yield products with a variety of morphologies, while reactions that are initially sulfur-poor (e) produce a consistent nanoparticle product (diameter=3.2±0.4 nm).

c,f) Corresponding Raman spectra from the four-component reactions shown in (b,e), from aliquots taken at 10 seconds and 30 minutes after the completion of precursor injection. Selected wavenumbers associated with known bulk modes from the intended AZTS product as well as binary (acanthite-like) and ternary (canfieldite-like) intermediates are indicated with dashed vertical lines. The spectra from the sulfur-poor reaction (f) are consistent with (mode-confined) AZTS products. By contrast, we observe clear Raman signals from binary/ternary impurities in reactions that are initially sulfur-rich (c), both initially and persisting 30 minutes after injection.

A stepwise reaction achieves ultra-small AZTS NCs

Building from these results, we considered strategies to mitigate the effect of large α-Ag_2S nanoplatelets to achieve the synthesis of phase-pure, ultra-small AZTS NC. For instance, increasing the temperature has been shown to speed the digestion of α-Ag_2S nanoplatelets.[72] Indeed, we note that previous syntheses of AZTS use elevated reaction temperatures (150-200 °C), which approach the polymorphic transition to argentite (β-Ag_2S) in the bulk system.[74] However, as we demonstrated above, reaction temperatures above 80 °C trigger the appreciable reduction of the silver precursor, which is detrimental to overall reaction control. Alternatively, prior work on the intentional synthesis of Ag_2S nanoparticles showed that an extended reaction time can remove large nanoplatelets.[71] We tested this, and confirmed that allowing the our sulfur-rich, α-Ag_2S-nanoplatelet-forming reaction to proceed at 80 °C for 30 minutes eliminates nanoplatelets and forms large Ag_2S nanoparticles (average size: 4.4 ± 0.5 nm, Figure S10a), likely through a non-classical growth mechanism.[72] However, when we subsequently converted these larger templates to AZTS, we could only obtain NCs that emit at wavelengths longer than 725 nm, consistent with large particles (Figure S10b). This aligns with the slow reaction kinetics that we observe in single-injection reactions to form AZTS NC, where infrared emission spectra at early times (*e.g.* 10s) prominently indicate the presence of α-Ag_2S nanoplatelets, but do not yet exhibit significant emission from quaternary AZTS (Figure S7a and b). Indeed, in single-injection reactions it took >15 minutes for the emission spectrum to predominantly resemble AZTS—with a peak at 780 nm that again pointed to large NC products (>4.5 nm) with relaxed quantum confinement (Figures 3a and b). Therefore, we concluded that an extended growth period can improve phase-purity, but it is counterproductive to achieving a small Ag_2S nanoparticle template (<3.5 nm) for the subsequent conversion to strongly confined AZTS NCs.

Instead, inspired on our study of the formation mechanism of quaternary Cu_2ZnSnS_4 NCs[24] and the reported morphologies of Ag_2S templates,[71-72, 75] we designed a synthetic route to yield smaller AZTS NCs with improve phase purity and better size and morphological control. Our approach was to manage the stepwise progression through the key intermediates—binary (Ag_2S) and ternary (ATS)—while suppressing both the formation of metallic Ag NPs as well as large α-Ag_2S nanoplatelets. With this aim, we developed and explored a synthetic route based on a non-conventional quadruple injection approach (Scheme 1, Figure S11). In the first step, we exploit sulfur-poor reaction conditions to access optimal Ag_2S templates. In the second step, we then supply Sn and additional S to form the ATS phase, targeting a clean transformation. As a final step, we add Zn to induce the complete conversion from ATS to pirquitasite (AZTS). We provide full details in Methods, but summarize the approach and results here.

Broadly, the Ag precursor in OLA is placed and heated in a flask before additional precursors are added *via* four consecutive injections within ~4 seconds. Rapid heating (12 °C/min) from the start of the reaction is essential to lessen the unwanted reduction of Ag^+. The first injection introduces a fifth of the total equivalents of sulfur in the form of TMS-S in toluene. As discussed previously, this has the advantage of allowing the Ag_2S template to form under sulfur-poor conditions at 80 °C. The next two injections (Sn^{4+}-OLA and additional TMS-S in toluene respectively) form the ATS phase and supply enough sulfur to satisfy the stoichiometry of the final AZTS product. The

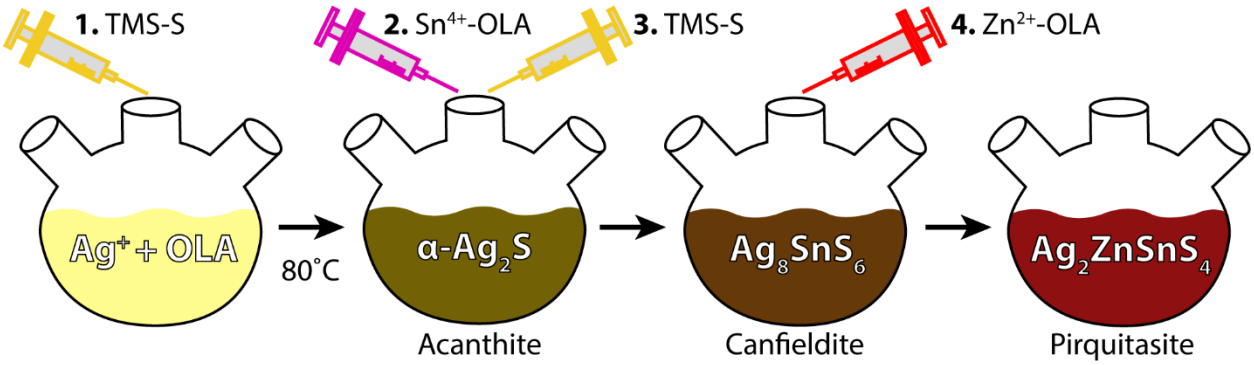

Scheme 1. Cartoon depicting the quadruple-injection sequence designed for the one-pot synthesis of Ag_2ZnSnS_4 nanocrystals to achieve sulfur-poor conditions for the initial formation of binary Ag_2S intermediates.

precursors for these effectively successive injections are kept separate to avoid the formation of Sn_xS impurities. Characterizing the synthesis at this point, we establish the formation of ternary ATS *via* a strong Raman signal at 309 cm^{-1} that matches a known mode for bulk canfieldite (Figure S12a), signatures of all three elements in XPS (Figure S12), and PXRD measurements that broadly match the reference pattern (Figure S12c).[76-77] Further, we confirm that the conversion is blocked if no additional TMS-S is added alongside the Sn (Figure S13). Thus, we consider that Sn^{4+} ions are added into the lattice along with at least two S^{2-} ions in order to meet the tetrahedral geometry of the ternary and quaternary phases, in a similar mechanism to that of Cu_2ZnSnS_4 NCs.[78-79] The last injection of Zn^{2+}-OLA generates the final quaternary AZTS product, which we confirm *via* Raman (Figure 2f, S14a), PXRD (Figure S14b), and elemental analysis (Supporting section 2-3). We found that a separate injection is needed, because injections of pre-mixed Sn and Zn precursors yield Ag_2S nanoparticles only, with no signs of AZTS emission (Figure S15). Lastly, we tested our strategy by performing the reverse quadruple injection, where the Zn precursor is injected before the Sn. We found that this only yields poorly emissive species that are not consistent with AZTS (Figure S16). This can also be understood by analogy to Cu_2ZnSnS_4 NCs,[78-79] due to the similar role of Sn^{4+} in facilitating the subsequent integration of Zn^{2+} through the addition of S^{2-} into the lattice.

To evaluate whether this quadruple-injection approach permitted the synthesis of ultra-small, phase-pure particles, we first focussed on reactions that were quenched 10 seconds after the final precursor injection. (See Methods) Following two-step size-selective centrifugation with ethanol antisolvent, TEM of the product revealed ultra-small NCs (2.1 ± 0.3 nm diameter λ_{em} = 650 nm, Figure 3a, c, and d). Despite the smaller particles, this relative size dispersity compares favourably to previous reports.[11] Raman measurements of the final product match AZTS, showing a strong signal at 345 cm^{-1}, associated to the A_1 mode (Figure S14a).[80] This signal is relatively broad, consistent with phonon confinement effects, and possible contributions from other known modes for this phase 298 cm^{-1} (A_1, very weak), 270 cm^{-1} (B_1, medium), and 216 cm^{-1} (E, weak).[80] No

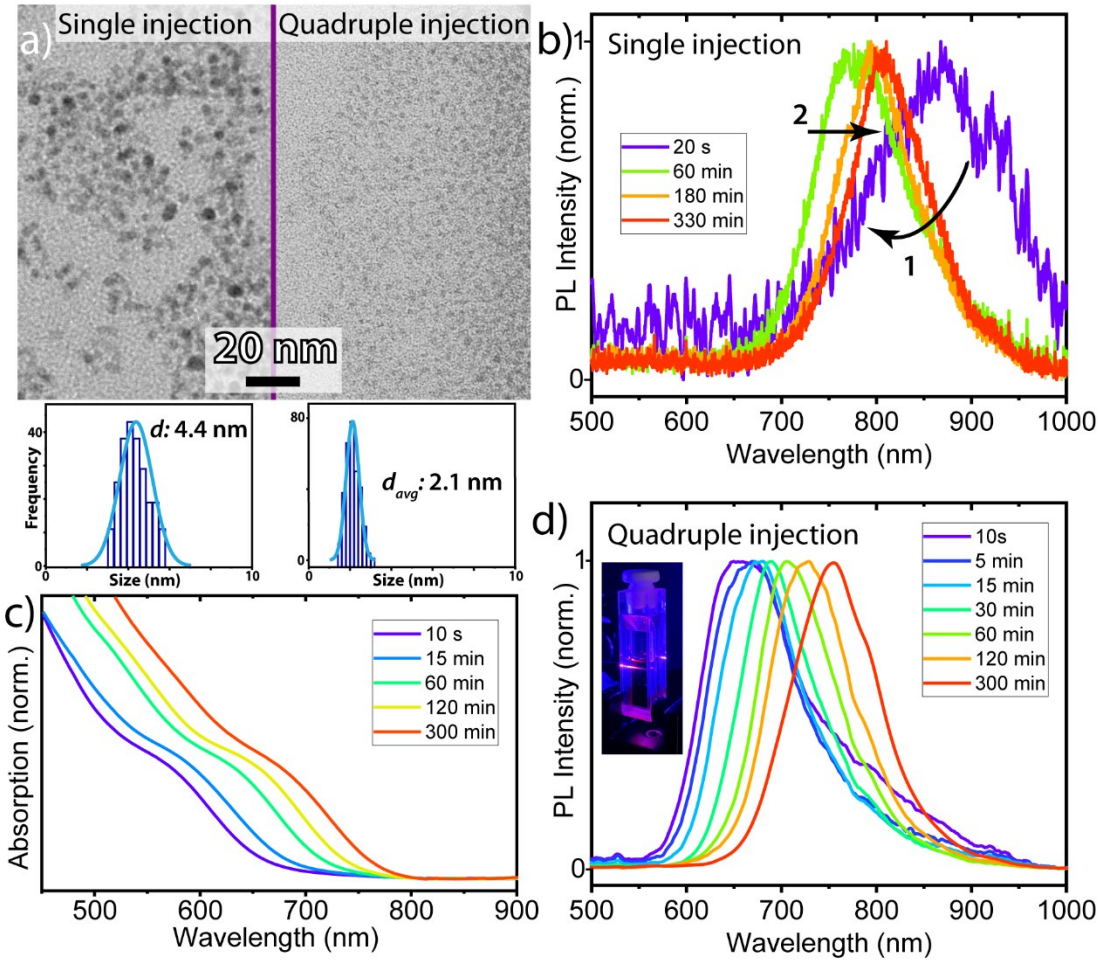

Figure 3. a) TEM images and associated sizing histograms of AZTS NCs synthesized at 80 °C through either a single-injection route (left image) or a quadruple-injection method (right image). The scale bar applies to both images.
b) Emission spectra of AZTS NCs from aliquots taken during single-injection synthesis. Initially, prominent emission peaked at λ: 880 nm is seen and attributed to α-Ag_2S nanoplatelets. The shortest-wavelength emission peak (λ: 780 nm) is observed 60 minutes after injection, corresponding to AZTS nanocrystals with diameters of 4.4±0.8 nm (Panel a, left images).
c) Optical absorption and d) emission spectra from aliquots tracking the quadruple-injection synthesis of AZTS NCs. NIR emission associated with Ag_2S is minimal, and we instead observe photoluminescence that smoothly shifts from λ: 650 to 750 nm, consistent with the growth of quantum-confined AZTS NCs. The first aliquot exhibits emission peaked at λ: 650 nm, which corresponds to low-dispersity, ultra-small AZTS NCs with diameters of 2.1±0.3 nm (Panel a, right images). (Inset) Photograph of emission from ultra-small AZTS NCs under λ: 450 nm excitation (natural-colour photo taken with an iPhone 11).

prominent impurity modes from ternary (Ag_8SnS_6, 309 cm^{-1})[64] or binary (Ag_2S 91 cm^{-1}, Sn_xS 218/318 cm^{-1}, ZnS 278/351 cm^{-1})[65, 81] species are observed, indicating a phase-pure AZTS product. PXRD diffractograms of the AZTS product are broadly consistent with the reference pattern for the tetragonal phase (Figure S14b). However, disambiguation from ternary ATS *via* XRD alone is challenging due to the considerable breadth of reflections from these NCs (which comprise 16 unit cells on average, unit cell parameters: a~1.1 and b=c~0.5 nm),[11] and the possible effects of *e.g.* nano-scale strain or a partially amorphous structure as observed in binary Ag_2S.[71, 73] We then evaluated the elemental composition of the final products through inductively coupled plasma optical emission spectroscopy (ICP-OES), X-ray photoelectron spectroscopy (XPS), and scanning electron microscopy – energy dispersive x-ray spectroscopy (SEM-EDS) (Table S1). Using SEM-EDS, we obtain a relative stoichiometry of $Ag_{2.5}Zn_{1.3}SnS_{4.5}$, which is in good agreement with bulk AZTS (Ag_2ZnSnS_4.) The other two techniques yield corroborating results (Table S1), once we account for probable elemental losses during sample preparation (Supplementary Section S2-3.) Interestingly, we observe a slight excess of Zn relative to Sn in SEM-EDS and XPS, and a slight deficit in XPS where the more-aggressive requisite sample cleaning could strip surface atoms.[82] Thus, our elemental analysis data is also consistent with a Zn-rich surface termination. Lastly, the elemental peak locations in XPS (Figure S6) are consistent with the expected oxidation state values for all elements in the quaternary product (*i.e.* Ag^+, Zn^{2+}, Sn^{4+}, and S^{2-}). Taken together, our TEM, XRD, Raman, and elemental analysis data confirm that we can obtain phase-pure, ultra-small AZTS NCs with improved size-dispersity *via* the quadruple-injection approach.

We then characterized the optical properties of the AZTS NCs synthesized through our quadruple-injection method. Optical absorption spectra show shoulders consistent with an excitonic feature with a peak wavelength that is <600 nm initially (*i.e.* 10 s after injection) and then progressively red-shifts towards λ: 700 nm over the reaction. (Figure 3c) This matches expectations for the growth of quantum-confined particles. Most notably, photoluminescence spectra from AZTS NCs obtained 10s after injection exhibit a prominent feature centered at 650 nm (Figure 3d). This is a considerably shorter emission wavelength than previous reports (*cf.* 740 nm),[11, 13] and is consistent with strong quantum confinement in ultra-small particles. The emission spectra also show a slight shoulder near 800 nm (consistent with Ag_2S, *vide supra*) that is observable in the 10s aliquot, but is no longer observed 5 minutes after injection. This agrees with the rapid formation of phase-pure AZTS from Ag_2S nanoparticles, which is corroborated by Raman spectra that show the growth of an intense AZTS peak (345 cm^{-1}) over this period. The shape and evolution of the optical spectra following the quadruple injection differ strongly from the single-injection reaction (Figure 3b). There, the feature near 650 nm is absent in the aliquot at 5 minutes (as well as earlier times when overall emission is very weak Figure S7a), and we instead see considerable photoluminescence beyond 800 nm. These observations match the expected effects of persistent, large α-Ag_2S nanoplatelets (*vide supra*), and demonstrate an advantage of the quadruple-injection approach.

Further, we find that the quadruple-injection strategy for AZTS NCs achieves phase and morphological purity at significantly lower reaction temperatures compared to the 140–220 °C used in previous reports.[11, 19-20, 62, 83] Indeed, we found that 80 °C was an optimal temperature to avoid the formation of impurity phases (*e.g.* Figure 2f, S17) while controllably obtaining small AZTS NCs *e.g.* average sizes between 2.1 ± 0.2 (Figure 3a) and 4.5 ± 0.6 nm (Figure S18),

corresponding to peak emission wavelengths between 650–790 nm (Figure 3d). We could controllably obtain larger NCs (*e.g.* 6.7 ± 0.8 nm, λ_{PL}: 820 nm) by injecting at 80 °C, and then increasing the temperature to 120 °C (Figure S19). In contrast, temperatures lower than 80 °C results in a much slower growth (Figure S20.) While we could detect the formation of ultra-small AZTS NCs at temperatures as low as 40 °C (Figure S20), Raman data shows that ATS impurities are already noticeable in the early time aliquots at 70 °C (Figure S21). Thus, when seeking the smallest particles *via* reactions quenched shortly after injection, we find that a temperature of 80 °C is optimal to ensure rapid, complete full conversion to the AZTS phase. Interestingly, a previous study on the solvothermal synthesis of macroscopic Ag_8SnS_6 crystals found that this related reaction also does not proceed at temperatures below 80 °C.[84] Taken as a whole, our data confirms that a quadruple-injection procedure allows access to smaller particles than previous reports, moving the short-wavelength bound of the emission range from 740 to 650 nm. We also show that this informed reaction design yields improved size-control and dispersity relative to single-injection syntheses, by efficiently guiding the conversion from Ag_2S to AZTS NCs through intermediate phases.

Understanding surface chemistry to improve the colloidal stability of AZTS NCs

We observe that the surface of AZTS NCs synthesized in OLA is highly sensitive to purification. For example, during washing, we find that the addition of ethanol antisolvent beyond the minimum required to form a pellet yields a precipitate that is not directly redispersible in toluene (See Methods). We interpret this as evidence for induced aggregation, which is consistent with a dynamic surface due to ligand self-exchange, as seen in other NCs passivated by OLA.[85-87] We sought information to aid the design of a surface passivation procedure that would better colloidally stabilize the small AZTS NCs (2.7 ± 0.4 nm, Figure S22) while enhancing their optical properties. Therefore, we used NMR experiments to understand the types of ligand binding at the surface. A key aspect of NMR experiments on NCs is that they can distinguish between bound and free-floating ligands because *e.g.* the limited mobility and slower tumbling of surface-anchored molecules leads to significant broadening of their ^{1}H NMR features relative to the same molecules in free solution[40, 88] (Supplementary Section 1.)

We first explored the surface of as-synthesized AZTS NCs with their native OLA ligands, dispersed in toluene-d_8. ^{1}H NMR experiments (Figure 4a) show the broadening of α-H (3 ppm), aliphatic protons (~1.4 ppm), and olefinic protons (5.55 ppm), relative to the same features in well-solvated (free) OLA. This indicates a degree of binding. Nonetheless, these features appear at lower ppm (*e.g.* olefinic at 5.55 ppm) compared to other NC systems where OLA and oleic acid (OA) are tightly bound (>5.60 ppm).[39, 89] This is additional circumstantial evidence that OLA on as-synthesized AZTS NCs is in a dynamic absorption/desorption exchange.

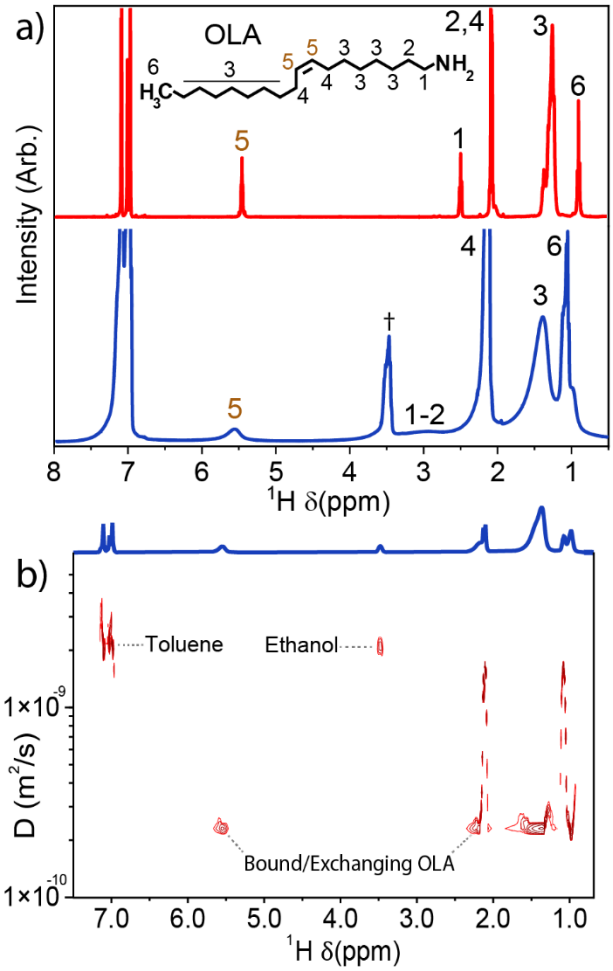

Figure 4. ^{1}H NMR characterization for as-synthesized AZTS NCs. a) 1D spectra of native NCs (blue trace) display resonances that correspond to the OLA reference spectrum (red trace), but are broadened. This is consistent with ligands bound to the surface of slowly-tumbling NCs, indicating that as-synthesized AZTS are passivated with OLA. †This feature arises from residual ethanol from purification.
b) Corresponding DOSY spectrum for native NCs show that OLA molecules diffuse more slowly than *e.g.* solvent molecules, corroborating OLA binding to the NC surface.

Further evidence for the dynamic binding of OLA species on AZTS NCs was provided by 2D NMR techniques. We first used diffusion-ordered spectroscopy (DOSY) to monitor the ^{1}H resonances associated with OLA (Figure 4b). Then, we used the Stokes-Einstein equation to extract a diffusion coefficient, D (230 μm^2·s^{-1}), which in turn equates to a solvodynamic diameter of 3.3 nm in toluene (See Section S3). This is smaller than the predicted size of the particles with OLA ligands (5.7-6.7 nm), taking the extended chain length as 1.5-2.0 nm.[90] However, these

ostensibly counterintuitive results are in line with previous reports on dynamic surface passivation, where the measured diffusion coefficient of amine ligands is an average over the exchanging populations of free and bound species.[38, 40] Then, we identified negative cross-peaks in the NOESY spectrum of native OLA AZTS NCs for the olefinic and aliphatic protons, indicating that the broadened resonances observed through ^{1}H NMR have negative NOE enhancements (Figure S23a). These peaks change sign in the ROESY spectrum, confirming that some ligands are indeed interacting with the surface (Figure S23b, and Supplementary Section 1). We also find weak, negative cross-peaks along the diagonal of the ROESY spectrum, showing that a portion of ligands are also undergoing an adsorption/desorption exchange.[42, 91-92] Taken together, our suite of NMR measurements corroborate our qualitative observations on the sensitivity of the NCs to purification, and we thus we conclude that the binding of OLA ligands to the surface of AZTS NCs is dynamic.

Our first attempt to understand the dynamic binding of OLA in as-synthesized AZTS NCs and ultimately generate tighter binding motifs was inspired by recent work on related materials. Specifically, while L-type binding for OLA is a common motif on semiconductor NCs, it was shown by Dierick (Hens) and co-workers that binding on the surface of $CuInS_2$ NCs is heterogeneous, and that shorter-chain, anionic impurities from the OLA solvent (*e.g.* OH^-) can bind to the surface.[93] These X-type impurity species could be removed *via* exchange with a different X-type ligand, such as a long-chained carboxylic acid, and this improved the colloidal stability of $CuInS_2$ NCs.[39]

For OLA-passivated AZTS NCs, we hypothesized that such short, molecular impurities (in addition to Cl^- ions from the Sn precursor) could be bound to the surface of as-synthesized AZTS NCs and contribute to their poor colloidal stability. Thus, we investigated an X-for-X exchange procedure by titrating OLA-passivated AZTS NCs (d: 2.7 nm) with undec-10-enoic acid (UDA). The distinct vinylic NMR resonance of UDA allows it to be readily distinguished from OLA.[33] We first observe using DOSY that the effective solvodynamic diameter of UDA treated AZTS is 1.3 nm—smaller than either the expected value for these AZTS NC with extended UDA ligands (5 nm), or that we previously measured for OLA (dynamically) bound to the NCs (3.3 nm) (Figure S24c and associated discussion.) This indicates that UDA is not irreversibly replacing X-type impurities, but instead becomes involved in a dynamic interaction with the surface. Further, we recognize clear evidence of NC aggregation at high UDA concentrations (Figure S25). We then identify that UDA can protonate OLA and form $OLAm^+$ species that can interact with the surface (Figure S24 and S25). This is consistent with the binding of X-type species within overall-neutral, ion-pair ligands (*e.g.* $OLAm^+$ UDA^-).[82, 94]

We then used steady-state and transient photoluminescence spectroscopy to give additional insight into the surface chemistry of OLA-passivated AZTS NCs exposed to X-type OA. Specifically, we added OA to a purified dispersion of OLA-passivated AZTS, using small concentrations that did not promote evident aggregation (*vide supra*, where *e.g.* 50:1 OA:OLA caused aggregation in <30 minutes). We observed that the post-synthetic addition of *e.g.* 10:1 OA:OLA caused an immediate, significant loss of the steady-state photoluminescence (Figure 5a). Similar PL quenching was seen when comparable small amounts of OA were added during synthesis (Figure S27). Figure 5b

shows that the post-synthetic addition of OA induced a progressive decrease in the average lifetime as a function of the amount of OA added (from 150 ± 10 to 70 ± 10 ns, determined *via* Reimann sum). Notably, AZTS NCs exhibit decay dynamics with a pronounced non-monoexponential character, and the lifetime reduction predominantly results from an enhancement of the early-time decay (t<100ns) (Figure 5b). Similar dynamics are commonly observed from core-only NCs, and phenomenologically attributed to the effects of carrier trapping to poorly-emissive surface states.[95-96]

A plausible passivation scheme that rationalizes these overall behaviours is if OA addition indirectly induces under-passivated surface sites by provoking the net desorption of (dynamically bound) L-type OLA *via* the formation $OLAm^+$-OA^- adducts. This acid-base interaction could either occur at the NC surface or in free solution, given that our NMR experiments (Figure 4b, S24c) indicate that both relevant species are dynamically bound. Still, we cannot rule out some minimal X-type (UDA^-) exchange with impurity-type ligands, and we discuss some possibilities in Supporting Section A. In sum, our experiments show that the addition of carboxylic acids perturbs the binding equilibrium with overall-negative repercussions on the colloidal stability and photoluminescence of AZTS NCs, generating surface trapping behaviour and inducing aggregation.

Seeking a less-disruptive ligand exchange procedure to enhance the colloidal stability of as-synthesized (OLA-passivated) AZTS NCs, we pursued an exchange with thiols. This choice of ligand was guided by previous reports on L-type interactions with Ag in both metallic and Ag_2Se NCs.[97-99] These studies demonstrated that thiols bound preferentially to silver, so long-chained thiols could replace dynamically bound OLA and increase the colloidal stability. In addition, long-chain alkylthiols have a much higher pK_a (~10.6)[100] compared to carboxylic acids (~4.5), which we expected would reduce the troublesome aggregation associated with formation of the ion-pair adducts discussed above.

We explored the binding of thiols to AZTS NCs *via* titration of 2-phenylethanethiol (PET), because it has recognizable features in ^{1}H NMR that allow it to be distinguished from OLA (Figure 6 and S28). The introduction of PET into the ligand shell can be seen through the broadening of both the signal in the aromatic region (7.2-7.8 ppm) and that of the alkyl protons (2.8 and 4.0 ppm, Figure 6a). Similar to UDA, titrations using PET also provoked a narrowing of the olefinic proton signal of OLA at ~5.6 ppm (from 46 to 27 Hz) and the emergence of clear signatures for free/dynamic OLA at 1.15 ppm (Figure S28). These observations are evidence of the displacement of OLA from the NC surface. NOESY measurements on these samples show negative cross peaks for PET while ROESY inverts their sign, confirming an interaction of PET with the NC surface (Figure S29a, b, Supplementary Section 1). Further evidence for L-for-L exchange (as opposed to mechanisms involving proton-transfer/charged species[38, 82]) is the absence of signatures of ammonium in all relevant ^{1}NMR measurements. (Figures S31 and S32) Thus, we conclude that PET replaces OLA on the surface of AZTS NCs.

Practically, PET exchanges significantly increased the colloidal stability of AZTS NCs compared to the as-synthesized product (with OLA-only passivation). For instance, the addition of PET permitted as many purification cycles with ethanol as desired, each generating highly dispersible and oily pellets (Figure S33b). This contrasted to the behaviour of as-synthesized AZTS NCs, where precipitation with ethanol results in a dryer pellet (Figure S33a) that was no longer redispersible (without additives) after two cycles. We also showed that post-synthetic addition of 1-dodecanethiol (DDT), a more-common NC ligand, also displaces OLA from AZTS NCs while avoiding aggregation (Figure S33). This is consistent with our expectations that thiol ligands are an attractive general motif to improve the colloidal stability of AZTS NCs.

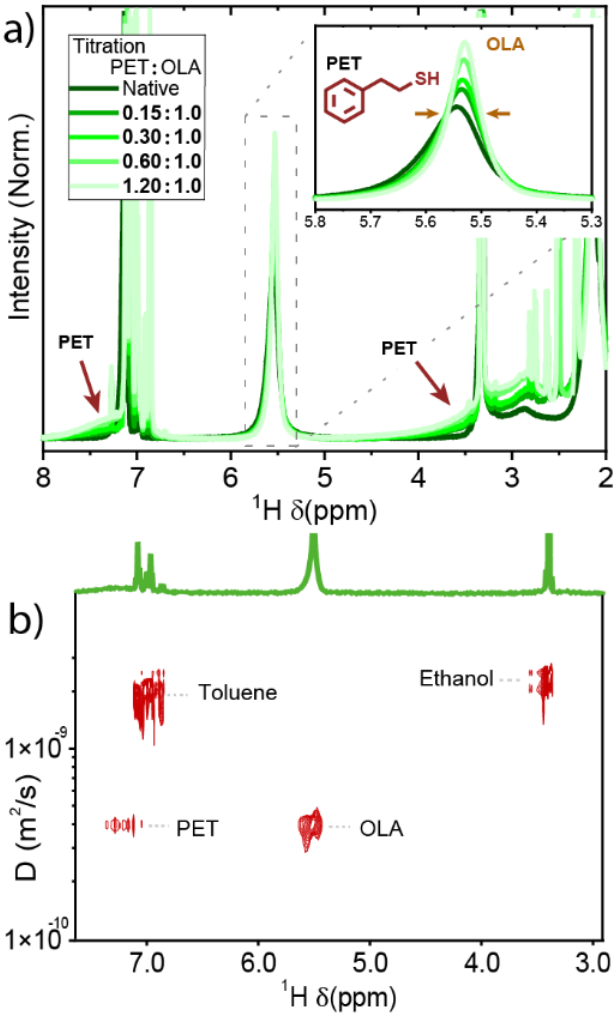

Figure 6. a) ^{1}H NMR characterization of AZTS NCs during titration with PET. The spectrum of as-synthesized (OLA-passivated) AZTS NCs is shown in dark green while the brightening colour progression tracks the addition of PET. Broad resonances at 3–4 and 7–8 ppm (underlying strong, narrow solvent peaks) are associated with PET (reference spectrum: Figure S28), and their breadth indicates binding to the NC surface. The olefinic peak of OLA near 5.5 ppm also progressively sharpens as PET is added (inset), reflecting a greater population of free OLA in solution following displacement.
b) Final DOSY spectra taken with excess PET (1.2:1.0 PET:OLA) show single diffusion coefficients for both OLA and PET that are slow relative to molecular solvents, but faster than expected for a NC of this size. This implies that both ligands are dynamically interacting with the NC surface.

Thiol exchanges also had a beneficial effect on the emissivity of AZTS NCs. For instance, as-synthesized particles ($\lambda_{peak,PL}$: 710 nm, diameter~3.2 nm) from our quadruple-injection procedure exhibited a photoluminescence quantum yield (PLQY) of 1.2±0.5%. This is comparable to, or slightly greater than, prior reports on (larger) unshelled AZTS NCs.[11] We then observed that the post-synthetic addition of thiols to OLA-passivated NCs enables a 70% relative enhancement of the emission intensity (Figure S34), corroborated by an increase in the PLQY (from 1.2±0.5% to 1.9±0.5%) and the average photoluminescence lifetime (from 150 ± 10 ns to 170 ± 10 ns, Figure S34c), an effect that again grows in over ~1 hour. Notably, this improvement largely flows from the decreased magnitude of the early-time decay (t<100ns), while the late-time dynamics (100-1500 ns) are not significantly affected. This is consistent with DDT ligands passivating/hindering the formation of surface traps (*c.f.* the deleterious effect of OA, Figure 5). In this model of the photophysical dynamics, the slower late-time dynamics (τ=290±10 ns) would reflect the sub-population of AZTS NCs that are trap-free—thus the intrinsic dynamics of the AZTS NC core. In many other NC materials, the development of effective shelling procedures has ultimately enabled the synthesis of batches of NCs where the ensemble photophysics closely reflect this intrinsic limit.[101-102] For this reason, we emphasize that the apparent photoluminescence lifetime of trap-free AZTS NCs is much longer than established materials such as CdSe or InP. This is consistent with a lower intrinsic non-radiative decay rate, which is both fundamentally intriguing and particularly advantageous in applications where the NC serves as a photosensitizer.[14, 103]

Despite the markedly improved colloidal stability of AZTS NCs treated with thiols, we found that these exchanges were partial and that thiol ligands displayed some residual dynamism in binding. For instance, even at the endpoint of our PET titrations (1.2:1.0 PET:OLA), DOSY spectra detect bound PET ligands (*i.e.* that exhibit effective diffusion coefficients of D = 320 $\mu m^2 \cdot s^{-1}$) but continue to display signatures of OLA with comparable diffusivity. This implies that populations of both molecules continue to interact with the (slowly diffusing) NCs. Further, the corresponding solvodynamic diameters for both ligands are only 2.3 nm (where the AZTS core diameter alone is 2.7 nm), again consistent with a degree of dynamic exchange between bound and free ligands.

Thus, having observed that this partial exchange of OLA with thiols already improved the colloidal stability of AZTS NCs, we attempted to drive the exchange to completion. We first tried to wash OLA-passivated NCs with excess PET and then to re-precipitate them by adding EtOH (see Methods). After five washes, the olefinic signal for OLA remained visible in the ^{1}H NMR spectrum (~5.5 ppm, Figure S35a), showing that this method does not fully remove OLA. Second, we tested a more aggressive procedure that was reported to replace tightly bound OLA with thiols on the surface of $CuInS_2$ NCs.[39] In brief, we dispersed OLA-passivated AZTS NCs in a mixture of toluene and excess PET, and heated the dispersion to 130 °C for 2 hours, followed by two purification cycles using EtOH (see Methods). However, the olefinic signal for OLA remained in ^{1}H NMR spectra of the product, indicating that full displacement of OLA was unsuccessful (Figure S35b). Lastly, we explored the direct addition of DDT during the quadruple-injection synthesis of AZTS NCs. However, the addition of 2:1 DDT:Ag to the reaction mixture promoted the formation of a white precipitate, and yielded products with broad emission (Figure S36). Analogous observations of insoluble, less-reactive species *in situ* have been previously linked to the formation of lamellar silver thiolate coordination polymers.[104-105]

Noting both the surprising persistence of some surface-bound OLA in thiol-exchanged AZTS NCs and their clearly improved colloidal stability relative to NCs with OLA-only passivation, we propose that multiple OLA binding motifs with differing strengths co-exist in the as-synthesized particles. Evidence of such two-site binding behaviour has been reported in other NC systems, including PbS and CdSe.[33, 106] From our experiments, we consider that one motif can participate in an L-for-L ligand exchange through which thiols largely displace the (dynamically bound) OLA. Even though thiol binding may not be irreversible (consistent with the residual dynamism in the DOSY measurements), this replacement could still improve colloidal stability because the L-type binding of thiols to silver has been shown to be stronger than that of OLA in Ag_2Se NCs samples.[99]

By contrast, the binding motif that leads to the fraction of tightly bound OLA on AZTS NCs is less clear. However, we speculate briefly given similarities to recent studies of surface chemistry of initially amine-passivated InP NCs.[38] Specifically, exposure of InP NCs to other ligands (*i.e.* carboxylic acids or thiols) shown to remove only ~half of surface-bound amines, similar to our observations on AZTS. Supported by calculations, it was thus proposed that the remaining amines on InP NCs were associated with energetically favourable/tightly-bound sites that involve under-coordinated indium atoms at facet-edges and apices. However, the correspondence between our observations on AZTS NCs and the behaviour of InP is not exact. Notably, L-for-L exchanges were not observed in InP and targeted experiments instead detected $OLAm^+$-X^- species following presumed proton transfer from the incoming thiol ligands, forming thiolates.[38] By contrast, we do not detect the formation of such charged molecular species when PET or DDT are added to AZTS NCs (Figure S28 and S32). Nevertheless, the broader concept from the InP work—that more-strongly bound sites for L-type binding can arise from local chemical environments—is likely transferrable to our multi-metallic NCs, where the gamut of chemical binding/co-ordination environments is still-larger. An alternative tightly bound motif—in which X^+-type $OLAm^+$ binds to multiple exposed sulfur atoms at the NC surface—was recently proposed for particular facets present at the edges of CdSe|CdS nanoplatelets.[87] We cannot rule out that an analogous configuration could give rise to some of the tightly-bound ligand fraction that we observe in AZTS NCs, chiefly because of the challenge in decisively detecting characteristic signatures of bound ammonium in ^1H NMR (Figure S24, S25.) However, this hypothesis is less consistent with our experiments, because our elemental analyses of AZTS NCs indicate a metal-rich composition (Figure S6), and we observe evidence of net ligand desorption when acidic protons are added to as-synthesized (OLA-only) AZTS NCs. (Figure 5, S30) As a result, we speculate that the sub-population of tightly-bound (but un-protonated) OLA molecules on AZTS NCs are associated with L-type binding to *e.g.* under-co-ordinated Ag, surface sites associated with Sn^{4+} or Zn^{2+}, or any metal atoms perturbed by interactions with X-type impurities.

Thus, in sum, we have shown that understanding of the surface is key to remedying the poor native colloidal stability of AZTS NCs through informed post-synthetic ligand exchange. We find that the native OLA ligands bind dynamically, but that the post-synthetic addition of X-type OA induces net ligand displacement, and an associated loss of colloidal stability and emissivity. By contrast, we show that thiols are an effective post-synthetic additive that improves the colloidal and photoluminescence properties of AZTS NCs, even the very small NCs now accessible *via* our quadruple-injection approach. We show using NMR that thiols (*e.g.* DDT, PET) can replace native

OLA ligands in AZTS NCs, which is consistent with previous findings in binary and ternary silver-containing NCs.[107-110] However, though thiols improve the macroscopic properties of AZTS NCs, we find that, microscopically, these exchanges are only partial, consistent with these multi-metallic particles having an energetically heterogenous surface. These experiments paint a picture of the surface of AZTS NCs, and we observed a correlation between treatments that colloidally stabilize/destabilize the particles and those that suppress/enhance rapid (<50 ns) PL quenching that we associate with carrier trapping at the surface. In this view of the photophysics, the slow, late-time photoluminescence dynamics of AZTS NCs reflect a notably long intrinsic excited-state lifetime. Thus, the markedly improved colloidal stability AZTS NCs upon thiol treatment stimulated efforts to employ these particles in an optoelectronic application.

AZTS Nanocrystals Sensitize Red-to-Blue Triplet-Fusion Upconversion:

Accordingly, we explored the ability of AZTS NCs to sensitize triplet-fusion upconversion. Our improved, ultra-small AZTS NCs are attractive for upconversion photochemistry,[14, 47] given their optical gap, the long (>100 ns) average lifetime of their photoexcitations, and their less-toxic material composition. Following leading reports,[51-52, 111] we designed a hybrid system where AZTS NCs absorb light and sensitize the spin-triplet state on exciton-extracting ligands. These 'transmitter' ligands are then expected to transfer triplets to free-floating acceptor/emitters *via* a Dexter-type mechanism (Scheme 2).[112] Specifically, we functionalized OLA/DDT-passivated AZTS NCs (~2.1 nm) with 9-anthracenecarboxylates (9-ACA$^-$) and added a standard triplet acceptor to the solution, diphenylanthracene (DPA, See Methods). Notably, the short-wavelength 'blue' emission from DPA (λ ~ 425 nm, $h\nu$ ~ 2.9 eV) has sufficient photon energy to initiate chemical reactions, for example by activation of a radical initiator.[14, 113-114]

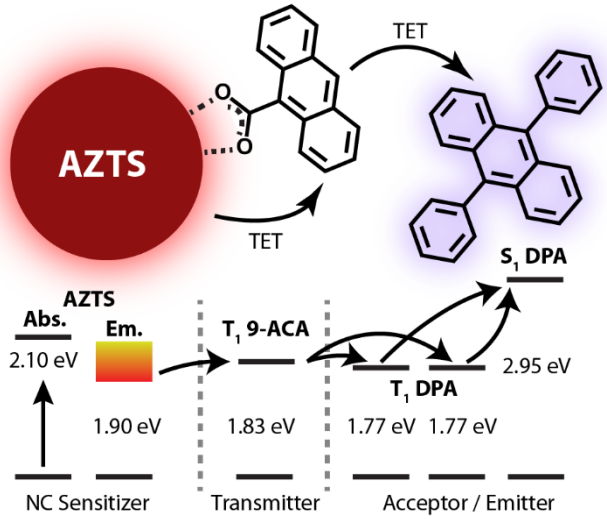

Scheme 2. Cartoon of the proposed upconversion mechanism. Red light ($\lambda_{ex.}$: 637 nm) is absorbed by AZTS NCs, and the energy from these photoexcitations is transferred to the spin-triplet state on surface-anchored 9-ACA$^-$ ligands. These triplets, in turn, transfer to free-floating DPA molecules. Triplet-state energies from ref. 51, and the 0-0 fluorescence peak is used to estimate the energy of the DPA S_1 (Figure S37). Energies for AZTS states are estimated from the emission peak, or the centroid of a gaussian fit to the long-wavelength shoulder of the excitonic absorption. Note that the binding motif of the 9-ACA$^-$ is representative only, as some X-type ligands may associate with the surface as charge-neutral ion pairs (Section 3)

Upon exciting deaerated solutions of this composite system with red light (λ_{ex}=637 nm), we observed blue emission (Figure 7a), showing a characteristic Franck-Condon progression and an overall peak at λ=425 nm that we associate with the 0-1 vibrational side-band of DPA (Figure 7b, Figure S37). This is strong evidence of upconversion *via* triplet sensitization and fusion, because blue emission is not observed under comparable conditions in incomplete assemblies that lack any of the AZTS NCs, the DPA, or the 9-ACA (Figure S38, Figure S39c). Thus, we conclude that ultra-small AZTS NCs can sensitize red-to-blue triplet fusion upconversion, adding a new member to the short list of solution-based upconversion schemes facilitated by less-toxic NC sensitizers.[56-57, 115-116]

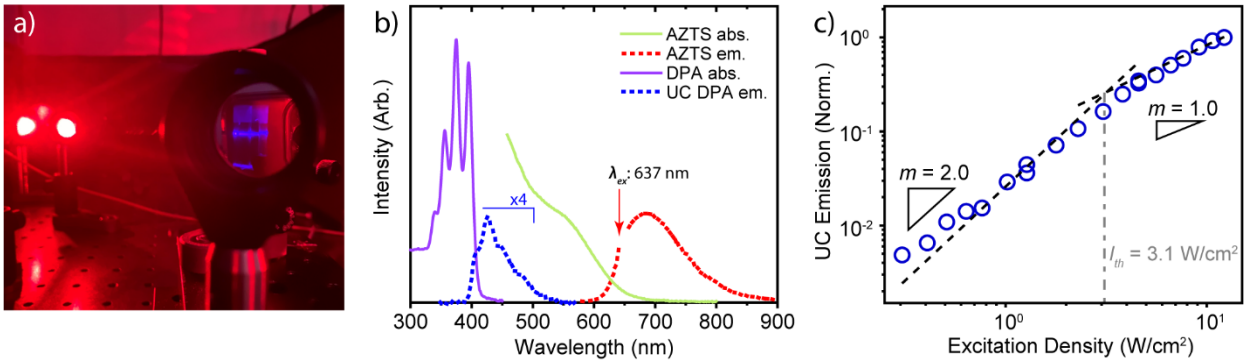

Figure 7. Triplet-fusion upconversion sensitized by AZTS NCs. a) Experiment setup viewed through a λ: 500 nm short-pass filter to show the upconverted blue light ($\lambda_{em.}$: 425 nm) (natural-colour photo taken with an iPhone 11.)
b) Steady-state absorption and emission spectra. The photoluminescence is collected from the complete system in solution (9-ACA-functionalized AZTS NCs and DPA, See Scheme 2, Methods) under $\lambda_{ex.}$: 637 nm excitation. Thus, it contains both direct emission from the AZTS NC and the upconverted emission from DPA molecules. The spectral region from 350–750 nm (re-coloured blue) has been magnified 4-fold to enhance visibility. The absorption spectra of the relevant materials in solution were measured separately.
c) Excitation-intensity–dependence of the upconverted emission, showing the characteristic quadratic-to-linear transition for triplet fusion beyond a threshold excitation intensity, I_{th}.

Additional photophysical studies are consistent with triplet sensitization mediated by 9-ACA bound to the surface of AZTS NCs. For instance, adding 0.5 eq 9-ACA under ambient (O_2-containing) atmosphere induces significantly more quenching than the same concentration of electronically-inactive OA (Figure S39a). This is consistent with 9-ACA quenching the AZTS *via* an additional mechanism (such as triplet transfer) that is beyond any non-specific net displacement of OLA by these two carboxylic acids acting as proton donors (*c.f.* Figure 5.) Then, we observe that the PL of un-functionalized AZTS NCs is neither significantly affected by exposure to O_2 (Figure S38a), nor DPA (Figure S39d). Accordingly, we consider that direct sensitization of either DPA triplets or singlet oxygen by photoexcited AZTS NCs is minimal. However, once AZTS NCs are treated with 9-ACA, we observe that the NC PL can be clearly quenched by either the subsequent addition of DPA (under Ar), or reversibly quenched and restored by exposure to ambient O_2 and re-sparging with Ar. Both of these observations are consistent with the extraction of NC photoexcitations onto surface-bound 9-ACA$^-$ transmitter ligands, [14, 51-52] and then further energy transfer to free-floating DPA (or O_2) molecules (Scheme 2.) These experiments do not meaningfully distinguish whether 9-ACA$^-$ is bound directly to metal atoms, or more-dynamically as overall charge-neutral ion pairs (See prior section.)

Lastly, Figure 7c displays the irradiance-dependence of the upconverted emission intensity from our AZTS-sensitized system, showing clear quadratic and linear regimes. This is further evidence of photoluminescence *via* triplet-fusion upconversion, which is expected to show a characteristic quadratic-to-linear transition with increasing excitation power as bimolecular fusion becomes the predominant recombination pathway for triplets.[117] Then, the threshold intensity (I_{th}) marking the quadratic-to-linear transition is a performance metric, because systems that achieve max-efficiency upconversion at lower intensities are advantageous in many applications.[3, 14, 51-52, 118] We extract I_{th}=3.1 W/cm^2 from the inflection point in our excitation-density–dependent measurements (Figure 7c), which is comparable to reported systems with less-toxic NC sensitizers.[56-57, 115-116] However, only one of these systems has generated photochemically-active deep-blue light (0-0 shoulder of DPA at λ: 415 nm) from red excitation (λ: 637 nm)[14]—thus achieving a beneficially larger anti-Stokes shift (ΔE=1.04 eV) relative to systems requiring yellow/green excitation (λ<590nm)—and our system breaks new ground with a threshold intensity more than 10x lower. Thus, our upconversion platform built on ultra-small AZTS NCs stands as a strong candidate among the rising tide of less-toxic NC-sensitized triplet-fusion systems.

Conclusions

We designed, implemented, and investigated an improved synthetic route to AZTS NCs, an underexplored, less-toxic material system attracting recent research interest. Our study was mechanistically motivated, seeking to suppress the reduction of Ag and the formation of α-Ag_2S nanoplatelets, and temporally separate the formation of binary (Ag_2S), ternary (Ag_8SnS_6), and quaternary (Ag_2ZnSnS_4) species. These intentions were inspired by our previous findings in the formation mechanism of quaternary Cu_2ZnSnS_4 NCs,[24] and the reported effect of sulfur stoichiometry on the morphologies of Ag_2S templates.[71-72] Overall, this adapted synthetic approach yielded AZTS nanomaterials that access a new, smaller size-range; exhibit enhanced colloidal stability; and possess superior photophysical properties that enabled a demonstration of triplet-fusion upconversion with AZTS NCs serving as the triplet sensitizer.

First, investigating the established reaction, we highlighted that a commonly employed solvent/ligand (OLA) can chemically reduce the silver precursor, particularly at elevated temperatures (>80 °C). This reduction can form metallic Ag NPs prior to sulfur injection (and the expected nucleation of metal-sulfide particles), ultimately yielding larger AZTS NCs with broader size distributions at reaction completion. Accordingly, we are able to obtain greater control in reactions run at low temperatures (~80 °C). Then, studying an OLA-based, one-pot synthesis of AZTS NCs at 80 °C, we identify that acanthite-like (Ag_2S) nanoparticles are a key intermediate species. We explored their formation, discovering that reactions with stoichiometric sulfur access small (<5 nm), pseudo-spherical Ag_2S nanoparticles that are superior templates for conversion to AZTS. By contrast, the excess sulfur that is naturally present in one-pot AZTS reactions provokes the formation of large α-Ag_2S nanoplatelets that then frustrate control of the size, and phase-purity of multinary end-products. We concluded that AZTS reactions could target the suppression of α-Ag_2S nanoplatelet intermediates by initially working under sulfur-poor conditions during the nucleation event.

These findings motivated our development of a stepwise, one-pot procedure to modulate the formation of AZTS NCs with the aim to achieve smaller particles—not accessible through a single hot-injection—with improved control of size, morphology, and phase purity. In our quadruple injection procedure, the initial sulfur stoichiometry is regulated to access optimal Ag_2S nanoparticle templates. These particles are next cleanly converted *in situ* to canfieldite-like (Ag_8SnS_6) ATS NCs *via* the injection of $SnCl_4$, and then the final, phase-pure AZTS product through the addition of $Zn(OAc)_2$. We map the evolution of these intermediates through *e.g.* Raman and optical spectroscopies, and characterize the final products *via e.g.* elemental analysis, PXRD, and TEM. Overall, we show that reactions that separate cation addition steps in time through a quadruple injection (*vs.* single injection) can yield AZTS NCs that are smaller (*e.g.* 2–4 nm, with emission λ: 650-740 nm) and have improved absolute size-dispersity (*e.g.* 2.1±0.3 nm) relative to previous reports, in reactions run at significantly lower temperatures (80 °C).

We then identified that the native ligand passivation of AZTS NCs from this procedure involved charge-neutral OLA, but was dynamic in nature. Thus, we used 1 and 2D ^{1}H NMR techniques to unravel the surface chemistry of AZTS NCs, seeking to design procedures to improve colloidal stability. We found that ligands with thiol head-groups can replace loosely-bound OLA ligands, granting improved colloidal stability such that the NCs can endure multiple purification cycles without noticeable aggregation. Interestingly, even aggressive thiol treatments did not completely displace native OLA, indicating a heterogeneous surface where some amine ligands are presumably more-tightly bound. Conversely, we found that ligand exchanges with carboxylic acids decrease the colloidal stability of AZTS NCs, while generating ammonium-based ion pair adducts. Accordingly, we proposed that this decreased colloidal stability reflects the induced loss of solubilizing OLA from weakly-bound sites on the NC surface, and we correspondingly attribute the observed quenching of AZTS NC PL upon OA addition to the exacerbation of carrier-trapping at the NC surface. Overall, our results illustrate that post-synthetic thiol treatments are an effective strategy to increase the colloidal stability of AZTS NCs, though their slightly improved PLQY remains modest. As a result, we recommend further study understanding of the surface chemistry of AZTS NCs and inform advanced surface-passivation and/or shelling procedures. Encouragingly, however, transient photoluminescence data show that the excited-state lifetime of these core-only AZTS NCs is already >100 ns, and our analysis implies that the intrinsic excited-state lifetime of trap-free AZTS NCs is longer still. This is consistent with a low, intrinsic non-radiative decay rate, which is especially advantageous in photosensitization.

Finally, we used our improved, less-toxic quaternary AZTS NCs in a demonstration of 'red-to-blue' triplet-fusion upconversion. Following functionalization with triplet-extracting 9-ACA ligands and the addition of molecular DPA annihilator/emitters in solution, we find that our hybrid system can effectively convert red light (λ_{ex} = 637 nm) to blue ($\lambda_{UC,PL}$~425 nm) photons. Thus AZTS NCs join the short list of more-sustainable nanomaterials capable of sensitizing photochemically relevant upconversion with a large anti-Stokes shift. This success highlights how informed synthetic design can grant improved control of the size, phase, and surface of less-toxic materials, and ultimately advance the use of underexplored nanomaterials in demanding photophysical applications.

Methods

Chemicals: Silver (I) acetate [Ag(OAc)] was purchased from Alfa Aesar. Zinc (II) acetate [$Zn(OAc)_2 \cdot 2\ H_2O$], tin (IV) chloride [$SnCl_4$, anhydrous], hexamethyldisilathiane [TMS-S], oleylamine (OLA, technical grade 70%, and >98% primary amines), oleic acid (OA, technical grade 90%), octylamine (OCTY, 99%), 1-octadecene (ODE, technical grade, 90%), 1-dodecanethiol (DDT), undec-10-enoic acid (UDA), 2-phenylethanethiol (PET), deuterated toluene (tol-d_8, 99%), deuterated benzene (c_6d_6, 99%), hexane (≥ 99%), toluene (99%), acetonitrile, and ethanol (95%) were purchased from Sigma Aldrich. All chemicals were used as received without further purification.

Synthetic & Sample Preparation:

Ag NP synthesis: Ag(OAc) (0.150 mmol) was placed in a 3-neck round-bottom flask with OLA (3 mL), degassed three times through vacuum-nitrogen cycles, and heated to 100 °C for 1 minute under nitrogen atmosphere. The solution was then cooled to room temperature, transferred to a 50 mL Falcon tube, and purified twice. Each purification step involved adding a 50:50 EtOH:MeOH antisolvent mixture and centrifuging the solution at 6000 rpm (4430 rcf) for 40 seconds to precipitate the nanoparticles. The supernatant was discarded, and the particles re-dispersed in toluene for the next wash, or further experiments. The OLA used for all experiments was technical grade (70%) unless stated otherwise. However, this solvent was degassed beforehand at 120 °C for 4 hours under vacuum to remove suspected carbamate impurities.

Ag_2S synthesis: A 15 mL 3-neck round-bottom flask is charged with Ag(OAc) (0.150 mmol) and OLA (5 mL). The solution is degassed through three cycles of vacuum-nitrogen and kept under a nitrogen atmosphere at room temperature. In the meantime, the TMS-S precursor solution was prepared inside a glovebox. A vial was loaded with toluene (1 mL) and TMS-S, 0.061, or 0.150 mmol for the sulfur-poor and sulfur-rich conditions, respectively. This solution was mixed and placed in a 3 mL plastic syringe. Then, the temperature of the silver precursor solution was quickly ramped (15 °C/min) to 80 °C and the TMS-S solution was injected. The heating mantle was quickly removed and the reaction flask was cooled to 35 °C over ~2 minutes by blowing cold air.

For purification, the crude solution (~7 mL) was transferred to a 50 mL Falcon tube and IPA (12 mL) and MeOH (4 mL) were added to initiate precipitation, followed by centrifugation at 4430 rcf for 40 seconds.. The supernatant was discarded, and the pellet was redispersed in toluene (1 mL). A second purification step was performed by adding IPA (~4 mL) and MeOH (1 mL), and centrifuging at 4430 rcf for 40 seconds. The final product was redispersed in toluene (2 mL) and stored under air for further characterization.

Standard Quadruple-Injection AZTS NC synthesis: A 15 mL 3-neck round-bottom flask was loaded with Ag(OAc) (25 mg, 0.150 mmol) and sealed with rubber septa. At the same time, one 20 mL scintillation vial was charged with $Zn(OAc)_2 \cdot 2\ H_2O$ (14 mg, 0.075 mmol), degassed (4 hours at 120 °C) OLA (1 mL) while stirring, and then placed in a sand bath at ~80 °C. Another 20 mL scintillation vial was loaded with degassed OLA (1 mL) and a stir bar and brought inside a N_2 glovebox to prepare the Sn precursor solution. A micropipette was used to add $SnCl_4$ (9 μL, 0.075 mmol) to this vial. It is important to tilt the vial (~45°) and deliver the $SnCl_4$ onto a dry spot at the bottom of the vial to prevent traces of water in the OLA from hydrolyzing inside of the pipette tip

and forming an inconvenient gel. The vial was then quickly capped and taken out of the glovebox. The Sn precursor solution was placed in the same sand bath as the zinc precursor to promote dissolution (~10 minutes). While the $SnCl_4$ dissolved, two TMS-S solutions were prepared in different 20 mL scintillation vials inside the glove box. The first solution [1] contained toluene (1 mL) and TMS-S (13 µL/0.061 mmol), while the second [2] was comprised of toluene (1 mL) and TMS-S (49 µL/0.232 mmol). Each solution was loaded into a labelled 3 mL plastic syringe and taken out of the glovebox. This completed the precursor preparation.

For the reaction, degassed OLA (3 mL) was added to the 3-neck round-bottom flask containing the Ag(OAc). This solution was degassed through three cycles of vacuum-nitrogen at room temperature and rapidly heated to 80 °C (12 °C/min) under nitrogen and stirring. As the silver solution reaches 65 °C, two 1 mL plastic syringes are loaded: one with the tin solution (Sn-OLA) and the other one with the zinc precursor (Zn-OLA), both fully dissolved and pale yellow in colour. An additional 14/20 rubber septum is pierced with all four syringes as seen in Figure S11. Once the silver solution reaches 75 °C, the heating mantle is removed as well as the existing septum on the flask under a positive nitrogen flow. This septum is quickly replaced by the one holding the four syringes with the precursor solutions. The quadruple injection happens once the reaction reaches 80 °C in the order: 1) TMS-S [1], 2) Sn-OLA, 3) TMS-S [2], and 4) Zn-OLA, with one second between injections.

In reactions where we sought to track the synthesis, the septa was removed and aliquots were taken as described below. In reactions targeting a single size, the flask was cooled (over ~2 minutes) by blowing cold air at the time chosen to arrest the reaction.

AZTS NCs are purified through a standard EtOH workup. Essentially, the crude solution (~7 mL) is transferred to a 50 mL Falcon tube and 7.5 mL of EtOH are added. This tube is centrifuged at 4430 rcf for 3 minutes. The pale yellow supernatant is discarded and the NCs are re-dispersed in 2 mL toluene. For subsequent cycles, only 1 mL EtOH was added before centrifugation. This was sufficient to initiate precipitation, and the resulting supernatants were generally colourless. Three total cycles are performed in the standard procedure. Exceptions are noted explicitly.

Intentional variations from this standard protocol (employed to highlight the effect of different synthetic parameters) are explicitly noted where relevant in the main text and supporting information. For instance, a control AZTS reaction where the Sn and Zn precursors were injected together (See Figure S15) was performed by following the standard reaction other than the following alteration to the injection steps: 1) TMS-S [1], 2) Sn-OLA + Zn-OLA (prepared separately but mixed and injected together), and 3) TMS-S [2]. In another example variant, the synthesis of ternary ATS NCs (See Figure S12) was performed by following the standard protocol, but omitting the final injection of the Zn precursor.

Taking aliquots to track syntheses: After the last injection (Zn-OLA), a timer is started and 300 µL aliquots are periodically taken using a micropipette. The aliquots are placed in room-temperature vials, quenched by the addition of 600 µL room-temperature EtOH, and centrifuged for 40 seconds at 4430 rcf. The supernatant is discarded and the NCs are re-dispersed in 300 µL toluene for further experiments. A second purification step with the minimal amount of EtOH is possible. However, we found that the slightest EtOH excess can induce NC aggregation. In practice, we recommend

adding a small amount of OLA between purification steps to retain colloidal stability (See the NMR purification procedure below for details).

Purification for ^{1}H NMR experiments on AZTS NCs: After the final injection [4], the reaction is left to cool at ambient temperature until it reaches 35 °C (~5 minutes), and it is transferred to a 50 mL Falcon tube to be purified using EtOH. The first crash uses 7.5 mL of EtOH and the solution is centrifuged at 4430 rcf for 3 minutes. The amounts of antisolvent used are crucial for an optimal purification, as we observed that excess EtOH results in the aggregation of the NCs and jellified pellet. However, for mildly over-crashed samples, the NCs can be re-dispersed by the addition of a small amount of OLA (20-200 µL). After the first purification step, the supernatant is discarded and the NCs are re-dispersed in toluene (500 µL) and degassed OLA (25 µL). The tube is vortexed for 2 min and EtOH is added dropwise with a glass Pasteur pipette (25 drops) until the dispersion becomes turbid. The solution is centrifuged at 4430 rcf for 20 seconds, the supernatant discarded, and the NCs re-dispersed in toluene (500 µL) and degassed OLA (15 µL). After the dispersion is vortexed for 2 min, 25 drops of ethanol are added once again until the solution becomes turbid, and the tube is centrifuged at 4430 rcf for 10 seconds. The pellet is dried under a nitrogen flow to remove solvent traces and immediately re-dispersed in tol-d_8 or c_6d_6 for ^{1}H NMR experiments.

^{1}H NMR titrations: Stock solution were prepared of the ligands to be exchanged. UDA was prepared at 20 mg/mL in tol-d_8 while PET was prepared in c_6d_6. The titrations were conducted through the sequential addition of 8, 24, 32, 64, 128, 256, and 512 µL of the stock solution into the NMR tube containing the full product yield of one standard AZTS NCs reaction in 650 µL of c_6d_6 at room temperature. For example, 8 µL are added for the first titration, followed by the addition of 24 µL (32 µL total), then 32 µL (64 µL total), and so forth. The tubes were shaken for 3 minutes between each measurement.

Preparation of Upconversion Solutions: The products of an entire, optimized AZTS synthesis (arrested *via* air-cooling immediately after injection to obtain small NCs, *vide supra*) are re-dispersed in 2 mL of toluene after purification. Then, 200 µL of this solution is mixed with 10 µL of DDT and stirred for 5 minutes at room temperature. The dispersion is gently purified using EtOH (see above, intentionally retaining some feint colour in the supernatant), centrifuged at 4430 rcf for 2 minutes, and re-dispersed in 200 µL of toluene. A 40 µL aliquot from this dispersion is diluted with 300 µL of toluene inside a quartz cuvette. Then 50 µL of a (1 mg/mL) solution of 9-ACA in toluene:acetonitrile (10:2) was added as along with 100 µL of a (10 mg/mL) solution of DPA in toluene. The cuvette was sealed with a rubber septum, wrapped in parafilm, and sparged with argon for 3 minutes before taking the emission measurements.

Characterization:

NMR: Nuclear magnetic resonance measurements were performed on either a 400 MHz Varian MercuryPlus NMR spectrometer or a 500 MHz Agilent DD2 NMR spectrometer. 1D ^{1}H NMR measurements were performed on the 400 MHz instrument, while 2D DOSY, NOESY, and ROESY experiments were executed on the 500 MHz spectrometer. NOESY spectra were acquired at 300 ms mixing time, while ROESY measurements were taken at 100 ms mixing time. The titrations using UDA, OCTY, DDT, and PET were performed directly in the NMR tubes (*vide supra*). We waited 5 minutes after ligand addition before taking the first measurement. All spectra were recorded at a 25 s delay time and 8 scans in either tol-d_8 or c_6d_6.

Transmission electron microscopy (TEM): Standard-resolution images were acquired using a Hitachi HT7700 microscope at 100 kV. 400-mesh copper grids (Pacific grid) were immersed in a dilute dispersion of NCs in toluene for 1 second and left to dry under air. For each sample, the Fiji imaging-processing distribution[119] of the ImageJ software was used to facilitate the generation of a size-histogram for 300-500 individual particles across three representative regions of the micrograph. Due to the low contrast of the smallest nanocrystals, the diameter of each spheroidal particle was determined by manually tracing a short line across its apparent width. The standard deviation of the resulting size-histogram was used as the stated uncertainty of the average size. We confirmed that this manual procedure gave comparable results to binarization and algorithmic determination of the equivalent diameter from the summed area for larger AZTS nanocrystals (diameter = 4.4 ± 0.5 nm, Figure S10), for which there was sufficient TEM contrast for threshold-binarization to effectively distinguish nanocrystal area from background noise.

Powder X-ray diffraction (PXRD): The samples were prepared by drop-casting a concentrated dispersion of NCs in 50/50 hexanes/toluene onto an amorphous silicon substrate, which was then allowed to dry under air. The spectra were obtained using a Bruker D8 Advance diffractometer with monochromatized Cu Kα radiation with a nickel filter (1 mm slit). The X-ray source power was set to 40 kV and 40 mA. The spectra were collected in 2θ with a step increment of 0.015° and scan speed of 0.1 s step^{-1}. The reflections were calibrated with a LaB_6 standard, and the data was processed with the XPert Highscore software.

Raman spectroscopy: The data was collected using a Bruker Senterra Raman microscope. A 532 nm diode laser at 2 mW power was used with a 50x objective and a 3–5 cm^{-1} resolution. Each spectrum was collected over a period of 30 seconds.

Steady-state absorption spectroscopy: Optical absorption spectra were taken on a Perkin Elmer Lambda 1050 UV/Vis spectrophotometer.

Steady-State Emission Spectroscopy: Photoluminescence spectra taken with a home-built set-up at λ=450 nm excitation using a pen-diode (ThorLabs CPS450) at 2.5 mW. Upconversion experiments were conducted using an externally driven λ=637 nm diode (ThorLabs, HL63133DG) at 60 mW focused to a ~228 μm radius spot, as measured using a knife-edge. The emission set-up involved an off-axis parabolic collimating mirror to direct the emission from the sample to a reflective fibre-coupler (ThorLabs PC12FC-P01), which was then sent to an OceanOptics Flame spectrometer.

Photoluminescence Quantum Yields: The samples were prepared by diluting AZTS NCs in hexanes until an optical density of 0.2 at λ=450 nm over a 1 cm path-length was achieved (measured by UV-Vis). An Edinburgh FLS5 fluorimeter with continuous Xenon lamp and an integrating sphere was used for the PLQY measurements. Excitation was at λ=450 nm.

Time-Resolved Spectroscopy: Emission lifetime measurements were acquired using a 470 nm pulsed laser diode (PicoQuant, LDH-D-C-470). The data was obtained employing a single photon avalanche diode (Micro Photon Devices, $PD-050-CTD) and PicoQuant HydraHarp 400 event timer with 32 ps bin widths. A repetition rate of 500 kHz was used to allow long-lived signals to decay.

Inductively-coupled plasma optical emission spectroscopy (ICP-OES): The full product yield of a standard AZTS reaction (quenched by air-cooling five minutes after injection) was then purified via three cycles of the standard EtOH/hexanes wash with centrifugation (*vide supra*, with the only difference being redispersion in hexanes rather than toluene.) The resulting pellet was redispersed in 2mL hexanes to serve as a stock solution for ICP-OES and SEM-EDS.

For ICP-OES, a 10 µL aliquot from the AZTS NC stock solution in hexanes was transferred into a 15 mL Falcon tube. Ethanol was added (200 µL) and the tube was centrifuged for 1 minute at 3904 rfc. The colourless supernatant was discarded, and the pellet was digested in 1 mL of high-purity HNO_3 overnight. The following day, the samples were diluted to a total volume of 10 mL with Milli-Q water for the analysis. The measurements were performed using iCAP 6300 DUO ICP-OES spectrometer (ThermoScientific). The optical lines used for each element were Ag (328 and 338 nm), Sn (189 nm), and Zn (206 and 213 nm).

Scanning electron microscopy – Energy dispersive X-ray spectroscopy (SEM-EDS): A 40 µL aliquot from the AZTS NC stock solution for elemental analysis (see methods for ICP-OES above) was transferred to a 15 mL Falcon tube. Ethanol (300 µL) was added and the tube was centrifuged for 1 minute at 3904 rcf. The colourless supernatant was discarded and the pellet was re-dispersed in 30 µL of hexanes. The NC dispersion was drop cast onto a silicon substrate and air-dried for analysis. The measurements were acquired using a HRSEM JEOL JSM-7500LA (JEOL, Tokyo, Japan) microscope with a Zeiss GeminiSEM 560 (Zeiss, Oberkochen, Germany) field-emission gun, operating at 25 kV acceleration voltage. Energy-dispersive spectroscopy (EDS, Oxford instruments X-Max, 80 mm^2) operating at 25 kV was used to evaluate the elemental ratios.

X-ray photoelectron spectroscopy (XPS): The full product yield of one standard AZTS reaction (quenched by air-cooling five minutes after injection) was purified through three standard cycles of precipitation using EtOH and centrifugation, with re-dispersion in hexanes (rather than the standard toluene) at each step. The ultimate product was then washed three additional times in an effort to reduce residual organic materials on the NC surface. For each of these washes, the pellet was re-dispersed in 1 mL hexanes and 1 mL EtOH was added to induce precipitation of the NCs, followed by centrifugation at 3904 rcf for 1 min in each cycle. The clear supernatant was discarded after each centrifugation and the final pellet (after the sixth wash overall) was dried under vacuum overnight.

Measurements were carried out using a Kratos Axis UltraDLD spectrometer (Kratos Analytical Ltd.) with a monochromated Al Kα X-ray source (hν = 1486.6 eV) operating at 20 mA and 15 kV. Each sample was grounded to the sample holder via copper tape to maximize its electrical conductivity. Wide-area scans were collected over an analysis area of 300 × 700 μm^2 at a photoelectron pass energy of 160 eV and energy step of 1 eV, while high-resolution spectra were collected at a photoelectron pass energy of 20 eV and an energy step of 0.1 eV. A take-off angle of 0° with respect to sample normal direction was used for all analyses. The differential electrical charging effects were neutralized. The spectra have been referenced to the adventitious carbon 1s peak at 284.8 eV. The spectra were analyzed with the CasaXPS software (Casa Software Ltd., version 2.3.24)[120] and the residual background was eliminated by the Shirley method.

Author Information

Corresponding Author
Mark W.B. Wilson: 0000-0002-1957-2979

E-mail: mark.w.b.wilson@utoronto.ca

Authors
Francisco Y. Villanueva: 0000-0003-1102-3382

Minhal Hasham: 0000-0003-2931-1665

Philippe B. Green: 0000-0002-7025-2006

Christian J. Imperiale: 0000-0001-9504-7394

Samihat Rahman: 0000-0003-3261-6398

Darcy. C. Burns: 0000-0001-5411-3930

Author Contributions

This research was initiated and performed by F.Y.V. under the supervision of M.W.B.W. M.H acquired time-resolved spectroscopic data and aided in the acquisition of steady-state spectroscopic data for upconversion measurements. P.B.G. assisted in performing and refining synthetic procedures. C.J.I. obtained and analyzed the power-dependent upconversion measurement. S.R. assisted with the acquisition and analysis of steady-state spectroscopy. D.C.B. provided support for 1 and 2D ^{1}H NMR experiments and their interpretation. The manuscript was written by F.Y.V. and M.W.B.W., with contributions of all authors, who have given approval to the final version of the manuscript.

Notes

The authors declare no competing financial interest.

Supporting information available: Additional information and experimental data.

Acknowledgements

FYV, MH, S.R., and MWBW acknowledge the support of the Natural Sciences and Engineering Research Council of Canada (NSERC) *via* RGPIN-2017-06666 & 2023-05041, as well as support for research infrastructure from the Canada Foundation for Innovation [JELF-35991], and the Ontario Research Fund [SIA-35991]. FYV acknowledges support from NSERC Canada Graduate Scholarship–Doctoral (CGS-D) and Walter C. Sumner Memorial Fellowships. MH acknowledges a QEII Graduate Scholarship in Science and Technology and an Anoush Khoshkish Scholarship. PBG acknowledges an Ontario Graduate Scholarship. CJI acknowledges an NSERC-PGS-D fellowship. SR acknowledges a Faculty of Arts & Science Top (FAST) Doctoral Fellowship. Electron microscopy analysis was performed at the Centre for Nanostructure Imaging (CNI) at the

University of Toronto. The authors thank Ilya Gourevich for his assistance with TEM measurements. XRD measurements were performed at the McGill Chemistry characterization Facility with the assistance of Hatem Titi. Raman spectroscopy was performed at the ANALEST facility in the Department of Chemistry at the University of Toronto. Elemental analysis and PLQY measurements were performed at the Italian Institute of Technology (IIT) in the Nanochemistry facility. ICP-OES was performed with the assistance of Filippo Drago. SEM-EDS was performed at IIT with the help of Luca Leoncino. XPS analyses were performed by Francesco De Boni at IIT.

References

1. Kagan, C. R.; Lifshitz, E.; Sargent, E. H.; Talapin, D. V., Building Devices from Colloidal Quantum Dots. *Science* **2016,** *353* (6302), aac5523.
2. Li, Y.; Hou, X.; Dai, X.; Yao, Z.; Lv, L.; Jin, Y.; Peng, X., Stoichiometry-Controlled InP-Based Quantum Dots: Synthesis, Photoluminescence, and Electroluminescence. *J. Am. Chem. Soc.* **2019,** *141* (16), 6448-6452.
3. Wu, M.; Congreve, D. N.; Wilson, M. W. B.; Jean, J.; Geva, N.; Welborn, M.; Van Voorhis, T.; Bulović, V.; Bawendi, M. G.; Baldo, M. A., Solid-State Infrared-to-Visible Upconversion Sensitized by Colloidal Nanocrystals. *Nature Photonics* **2016,** *10* (1), 31-34.
4. Medintz, I. L.; Stewart, M. H.; Trammell, S. A.; Susumu, K.; Delehanty, J. B.; Mei, B. C.; Melinger, J. S.; Blanco-Canosa, J. B.; Dawson, P. E.; Mattoussi, H., Quantum-Dot/Dopamine Bioconjugates Function as Redox Coupled Assemblies for In Vitro and Intracellular pH Sensing. *Nat. Mater* **2010,** *9* (8), 676-684.
5. Grim, J. Q.; Manna, L.; Moreels, I., A Sustainable Future for Photonic Colloidal Nanocrystals. *Chem. Soc. Rev.* **2015,** *44* (16), 5897-5914.
6. Chopra, S. S.; Theis, T. L., Comparative Cradle-to-Gate Energy Assessment of Indium Phosphide and Cadmium Selenide Quantum Dot Displays. *Environ. Sci. Nano* **2017,** *4* (1), 244-254.
7. Wang, W.; Winkler, M. T.; Gunawan, O.; Gokmen, T.; Todorov, T. K.; Zhu, Y.; Mitzi, D. B., Device Characteristics of CZTSSe Thin-Film Solar Cells with 12.6% Efficiency. *Adv. Energy Mater.* **2014,** *4* (7), 1301465.
8. Kattan, N. A.; Griffiths, I. J.; Cherns, D.; Fermín, D. J., Observation of Antisite Domain Boundaries in Cu_2ZnSnS_4 by Atomic-Resolution Transmission Electron Microscopy. *Nanoscale* **2016,** *8* (30), 14369-14373.
9. Bourdais, S.; Choné, C.; Delatouche, B.; Jacob, A.; Larramona, G.; Moisan, C.; Lafond, A.; Donatini, F.; Rey, G.; Siebentritt, S.; Walsh, A.; Dennler, G., Is the Cu/Zn Disorder the Main Culprit for the Voltage Deficit in Kesterite Solar Cells? *Adv. Energy Mater.* **2016,** *6* (12), 1502276.
10. Wang, A.; He, M.; Green, M. A.; Sun, K.; Hao, X., A Critical Review on the Progress of Kesterite Solar Cells: Current Strategies and Insights. *Adv. Energy Mater. n/a* (n/a), 2203046.
11. Saha, A.; Figueroba, A.; Konstantatos, G., Ag_2ZnSnS_4 Nanocrystals Expand the Availability of RoHS Compliant Colloidal Quantum Dots. *Chem. Mater.* **2020,** *32* (5), 2148-2155.
12. Ma, C.; Guo, H.; Zhang, K.; Yuan, N.; Ding, J., Fabrication of p-type Kesterite Ag_2ZnSnS_4 Thin Films with a High Hole Mobility. *Mater. Lett.* **2017,** *186*, 390-393.
13. Saha, A.; Konstantatos, G., Ag2ZnSnS4–ZnS Core–Shell Colloidal Quantum Dots: A Near-Infrared Luminescent Material Based on Environmentally Friendly Elements. *Journal of Materials Chemistry C* **2021,** *9* (17), 5682-5688.
14. Imperiale, C. J.; Green, P. B.; Hasham, M.; Wilson, M. W. B., Ultra-Small PbS Nanocrystals as Sensitizers for Red-to-Blue Triplet-Fusion Upconversion. *Chem. Sci.* **2021,** *12* (42), 14111-14120.
15. Konstantatos, G.; Howard, I.; Fischer, A.; Hoogland, S.; Clifford, J.; Klem, E.; Levina, L.; Sargent, E. H., Ultrasensitive Solution-Cast Quantum Dot Photodetectors. *Nature* **2006,** *442* (7099), 180-183.
16. Mahboub, M.; Huang, Z.; Tang, M. L., Efficient Infrared-to-Visible Upconversion with Subsolar Irradiance. *Nano Lett.* **2016,** *16* (11), 7169-7175.

17. Yan, B.; Liu, X.; Lu, W.; Feng, M.; Yan, H.-J.; Li, Z.; Liu, S.; Wang, C.; Hu, J.-S.; Xue, D.-J., Indoor Photovoltaics Awaken the World's First Solar Cells. *Science Advances* **2022,** *8* (49), eadc9923.
18. Peng, Y.; Huq, T. N.; Mei, J.; Portilla, L.; Jagt, R. A.; Occhipinti, L. G.; MacManus-Driscoll, J. L.; Hoye, R. L. Z.; Pecunia, V., Lead-Free Perovskite-Inspired Absorbers for Indoor Photovoltaics. *Adv. Energy Mater.* **2021,** *11* (1), 2002761.
19. Hu, X.; Pritchett-Montavon, S.; Handwerker, C.; Agrawal, R., Reaction Pathways and Optoelectronic Characterization of Single-Phase Ag_2ZnSnS_4 Nanoparticles. *J. Mater. Res.* **2019,** *34* (22), 3810-3818.
20. Sasamura, T.; Osaki, T.; Kameyama, T.; Shibayama, T.; Kudo, A.; Kuwabata, S.; Torimoto, T., Solution-Phase Synthesis of Stannite-Type Ag_2ZnSnS_4 Nanoparticles for Application to Photoelectrode Materials. *Chem. Lett.* **2012,** *41* (9), 1009-1011.
21. Li, K.; Chai, B.; Peng, T.; Mao, J.; Zan, L., Synthesis of Multicomponent Sulfide Ag_2ZnSnS_4 as an Efficient Photocatalyst for H_2 Production Under Visible Light Irradiation. *RSC Adv.* **2013,** *3* (1), 253-258.
22. Burton, L. A.; Colombara, D.; Abellon, R. D.; Grozema, F. C.; Peter, L. M.; Savenije, T. J.; Dennler, G.; Walsh, A., Synthesis, Characterization, and Electronic Structure of Single-Crystal SnS, Sn_2S_3, and SnS_2. *Chem. Mater.* **2013,** *25* (24), 4908-4916.
23. Tan, J. M. R.; Lee, Y. H.; Pedireddy, S.; Baikie, T.; Ling, X. Y.; Wong, L. H., Understanding the Synthetic Pathway of a Single-Phase Quarternary Semiconductor Using Surface-Enhanced Raman Scattering: A Case of Wurtzite Cu_2ZnSnS_4 Nanoparticles. *J. Am. Chem. Soc.* **2014,** *136* (18), 6684-6692.
24. Yarur Villanueva, F.; Green, P. B.; Qiu, C.; Ullah, S. R.; Buenviaje, K.; Howe, J. Y.; Majewski, M. B.; Wilson, M. W. B., Binary $Cu_{2-x}S$ Templates Direct the Formation of Quaternary Cu_2ZnSnS_4 (Kesterite, Wurtzite) Nanocrystals. *ACS Nano* **2021,** *15* (11), 18085-18099.
25. Son, D. H.; Hughes, S. M.; Yin, Y.; Paul Alivisatos, A., Cation Exchange Reactions in Ionic Nanocrystals. *Science* **2004,** *306* (5698), 1009-1012.
26. Steimle, B. C.; Fenton, J. L.; Schaak, R. E., Rational Construction of a Scalable Heterostructured Nanorod Megalibrary. *Science* **2020,** *367* (6476), 418-424.
27. Heppke, E. M.; Mahadevan, S.; Bredow, T.; Lerch, M., Crystal Structure of Mechanochemically Prepared Ag_2FeGeS_4. *Z. Naturforschung B.* **2021,** *76* (10-12), 607-614.
28. Hinterding, S. O. M.; Berends, A. C.; Kurttepeli, M.; Moret, M.-E.; Meeldijk, J. D.; Bals, S.; van der Stam, W.; de Mello Donega, C., Tailoring Cu^+ for Ga^{3+} Cation Exchange in $Cu_{2-x}S$ and $CuInS_2$ Nanocrystals by Controlling the Ga Precursor Chemistry. *ACS Nano* **2019,** *13* (11), 12880-12893.
29. Steimle, B. C.; Lord, R. W.; Schaak, R. E., Phosphine-Induced Phase Transition in Copper Sulfide Nanoparticles Prior to Initiation of a Cation Exchange Reaction. *J. Am. Chem. Soc.* **2020,** *142* (31), 13345-13349.
30. Moreels, I.; Fritzinger, B.; Martins, J. C.; Hens, Z., Surface Chemistry of Colloidal PbSe Nanocrystals. *J. Am. Chem. Soc.* **2008,** *130* (45), 15081-15086.
31. Ong, W.-L.; Rupich, S. M.; Talapin, D. V.; McGaughey, A. J. H.; Malen, J. A., Surface Chemistry Mediates Thermal Transport in Three-Dimensional Nanocrystal Arrays. *Nat. Mater* **2013,** *12* (5), 410-415.
32. Owen, J., The Coordination Chemistry of Nanocrystal Surfaces. *Science* **2015,** *347* (6222), 615-616.

33. Green, P. B.; Yarur Villanueva, F.; Imperiale, C. J.; Hasham, M.; Demmans, K. Z.; Burns, D. C.; Wilson, M. W. B., Directed Ligand Exchange on the Surface of PbS Nanocrystals: Implications for Incoherent Photon Conversion. *ACS Appl. Nano Mater.* **2021,** *4* (6), 5655-5664.
34. Drijvers, E.; De Roo, J.; Martins, J. C.; Infante, I.; Hens, Z., Ligand Displacement Exposes Binding Site Heterogeneity on CdSe Nanocrystal Surfaces. *Chem. Mater.* **2018,** *30* (3), 1178-1186.
35. Kessler, M. L.; Dempsey, J. L., Mapping the Topology of PbS Nanocrystals Through Displacement Isotherms of Surface-Bound Metal Oleate Complexes. *Chem. Mater.* **2020,** *32* (6), 2561-2571.
36. Majetich, S. A.; Carter, A. C.; Belot, J.; McCullough, R. D., ^{1}H NMR Characterization of the CdSe Nanocrystallite Surface. *J. Phys. Chem.* **1994,** *98* (51), 13705-13710.
37. Kessler, M. L.; Kelm, J. E.; Starr, H. E.; Cook, E. N.; Miller, J. D.; Rivera, N. A.; Hsu-Kim, H.; Dempsey, J. L., Unraveling Changes to PbS Nanocrystal Surfaces Induced by Thiols. *Chem. Mater.* **2022,** *34* (4), 1710-1721.
38. Leemans, J.; Dümbgen, K. C.; Minjauw, M. M.; Zhao, Q.; Vantomme, A.; Infante, I.; Detavernier, C.; Hens, Z., Acid–Base Mediated Ligand Exchange on Near-Infrared Absorbing, Indium-Based III–V Colloidal Quantum Dots. *J. Am. Chem. Soc.* **2021,** *143* (11), 4290-4301.
39. Dierick, R.; Van den Broeck, F.; De Nolf, K.; Zhao, Q.; Vantomme, A.; Martins, J. C.; Hens, Z., Surface Chemistry of CuInS2 Colloidal Nanocrystals, Tight Binding of L-Type Ligands. *Chemistry of Materials* **2014,** *26* (20), 5950-5957.
40. Hens, Z.; Martins, J. C., A Solution NMR Toolbox for Characterizing the Surface Chemistry of Colloidal Nanocrystals. *Chemistry of Materials* **2013,** *25* (8), 1211-1221.
41. Keeler, J., *Understanding NMR Spectroscopy*. Wiley: 2002; p Ch8.
42. Neuhaus, D.; Williamson, M. P. In *The Nuclear Overhauser Effect in Structural and Conformational Analysis*, Wiley-VCH: 2000.
43. Burns, D. C.; Reynolds, W. F., *Optimizing NMR Methods for Structure Elucidation: Characterizing Natural Products and Other Organic Compounds*. Royal Society of Chemistry: 2018.
44. Claridge, T. D. W., *High-Resolution NMR Techniques in Organic Chemistry*. Elsevier Science: 2009.
45. Zhou, J.; Liu, Q.; Feng, W.; Sun, Y.; Li, F., Upconversion Luminescent Materials: Advances and Applications. *Chem. Rev.* **2015,** *115* (1), 395-465.
46. Sanders, S. N.; Schloemer, T. H.; Gangishetty, M. K.; Anderson, D.; Seitz, M.; Gallegos, A. O.; Stokes, R. C.; Congreve, D. N., Triplet Fusion Upconversion Nanocapsules for Volumetric 3D Printing. *Nature* **2022,** *604* (7906), 474-478.
47. Ravetz, B. D.; Pun, A. B.; Churchill, E. M.; Congreve, D. N.; Rovis, T.; Campos, L. M., Photoredox Catalysis Using Infrared Light *Via* Triplet Fusion Upconversion. *Nature* **2019,** *565* (7739), 343-346.
48. Okumura, K.; Mase, K.; Yanai, N.; Kimizuka, N., Employing Core-Shell Quantum Dots as Triplet Sensitizers for Photon Upconversion. *Chem. Eur. J.* **2016,** *22* (23), 7721-7726.
49. Gray, V.; Dzebo, D.; Abrahamsson, M.; Albinsson, B.; Moth-Poulsen, K., Triplet–Triplet Annihilation Photon-Upconversion: Towards Solar Energy Applications. *PCCP* **2014,** *16* (22), 10345-10352.
50. Islangulov, R. R.; Kozlov, D. V.; Castellano, F. N., Low Power Upconversion Using MLCT Sensitizers. *Chem. Commun.* **2005,** (30), 3776-3778.

51. Huang, Z.; Li, X.; Mahboub, M.; Hanson, K. M.; Nichols, V. M.; Le, H.; Tang, M. L.; Bardeen, C. J., Hybrid Molecule–Nanocrystal Photon Upconversion Across the Visible and Near-Infrared. *Nano Lett.* **2015,** *15* (8), 5552-5557.
52. Mongin, C.; Garakyaraghi, S.; Razgoniaeva, N.; Zamkov, M.; Castellano, F. N., Direct Observation of Triplet Energy Transfer from Semiconductor Nanocrystals. *Science* **2016,** *351* (6271), 369-372.
53. Nienhaus, L.; Wu, M.; Bulović, V.; Baldo, M. A.; Bawendi, M. G., Using Lead Chalcogenide Nanocrystals as Spin Mixers: A Perspective on Near-Infrared-to-Visible Upconversion. *Dalton Trans.* **2018,** *47* (26), 8509-8516.
54. Weiss, R.; VanOrman, Z. A.; Sullivan, C. M.; Nienhaus, L., A Sensitizer of Purpose: Generating Triplet Excitons with Semiconductor Nanocrystals. *ACS Materials Au* **2022,** *2* (6), 641-654.
55. Gholizadeh, E. M.; Prasad, S. K. K.; Teh, Z. L.; Ishwara, T.; Norman, S.; Petty, A. J.; Cole, J. H.; Cheong, S.; Tilley, R. D.; Anthony, J. E.; Huang, S.; Schmidt, T. W., Photochemical Upconversion of Near-Infrared Light from Below the Silicon Bandgap. *Nat. Photon* **2020,** *14* (9), 585-590.
56. Han, Y.; He, S.; Luo, X.; Li, Y.; Chen, Z.; Kang, W.; Wang, X.; Wu, K., Triplet Sensitization by "Self-Trapped" Excitons of Nontoxic $CuInS_2$ Nanocrystals for Efficient Photon Upconversion. *J. Am. Chem. Soc.* **2019,** *141* (33), 13033-13037.
57. Liang, W.; Nie, C.; Du, J.; Han, Y.; Zhao, G.; Yang, F.; Liang, G.; Wu, K., Near-Infrared Photon Upconversion and Solar Synthesis Using Lead-Free Nanocrystals. *Nat. Photon* **2023,** *17* (4), 346-353.
58. Man, R. W. Y.; Brown, A. R. C.; Wolf, M. O., Mechanism of Formation of Palladium Nanoparticles: Lewis Base Assisted, Low-Temperature Preparation of Monodisperse Nanoparticles *Angew. Chem. Int. Ed.* **2012,** *51* (45), 11390-11390.
59. Wei, J.; Schaeffer, N.; Pileni, M.-P., Ag Nanocrystals: 1. Effect of Ligands on Plasmonic Properties. *J. Phys. Chem. B* **2014,** *118* (49), 14070-14075.
60. Jang, K.; Kim, S. Y.; Park, K. H.; Jang, E.; Jun, S.; Son, S. U., Shape-Controlled Synthesis of Silver Sulfide Nanocrystals by Understanding the Origin of Mixed-Shape Evolution. *Chem. Commun.* **2007,** (43), 4474-4476.
61. Wang, D.; Xie, T.; Peng, Q.; Li, Y., Ag, Ag_2S, and Ag_2Se Nanocrystals: Synthesis, Assembly, and Construction of Mesoporous Structures. *J. Am. Chem. Soc.* **2008,** *130* (12), 4016-4022.
62. Nagaoka, A.; Yoshino, K.; Kakimoto, K.; Nishioka, K., Phase Diagram of the Ag_2SnS_3–ZnS Pseudobinary System for Ag_2ZnSnS_4 Crystal Growth. *J. Cryst. Growth* **2021,** *555*, 125967.
63. Ning, J.; Zou, B., Controlled Synthesis, Formation Mechanism, and Applications of Colloidal Ag_8SnS_6 Nanoparticles and Ag_8SnS_6/Ag_2S Heterostructured Nanocrystals. *J. Phys. Chem. C* **2018,** *122* (12), 6566-6572.
64. Cheng, K.-W.; Tsai, W.-T.; Wu, Y.-H., Photo-Enhanced Salt-Water Splitting Using Orthorhombic Ag_8SnS_6 Photoelectrodes in Photoelectrochemical Cells. *J. Power Sources* **2016,** *317*, 81-92.
65. Martína, I.; Wiesinger, R.; Jembrih-Simbürger, D.; Schreiner, M. In *Micro-Raman Characterisation of Silver Corrosion Products: Instrumental Set Up and Reference Database*, 2012.
66. Ding, C.; Huang, Y.; Shen, Z.; Chen, X., Synthesis and Bioapplications of Ag_2S Quantum Dots with Near-Infrared Fluorescence. *Adv. Mater.* **2021,** *33* (32), 2007768.

67. Jeong, S.; Han, J. H.; Jang, J.-t.; Seo, J.-w.; Kim, J.-G.; Cheon, J., Transformative Two-Dimensional Layered Nanocrystals. *J. Am. Chem. Soc.* **2011,** *133* (37), 14500-14503.
68. De Trizio, L.; Gaspari, R.; Bertoni, G.; Kriegel, I.; Moretti, L.; Scotognella, F.; Maserati, L.; Zhang, Y.; Messina, G. C.; Prato, M.; Marras, S.; Cavalli, A.; Manna, L., $Cu_{3-x}P$ Nanocrystals as a Material Platform for Near-Infrared Plasmonics and Cation Exchange Reactions. *Chem. Mater.* **2015,** *27* (3), 1120-1128.
69. Butterfield, A. G.; Alameda, L. T.; Schaak, R. E., Emergence and Control of Stacking Fault Formation during Nanoparticle Cation Exchange Reactions. *J. Am. Chem. Soc.* **2021,** *143* (4), 1779-1783.
70. Li, Q.; Ding, Y.; Liu, X.; Qian, Y., Preparation of Ternary I-IV-VI Nanocrystallines *Via* a Mild Solution Route. *Mater. Res. Bull.* **2001,** *36* (15), 2649-2656.
71. Zhang, R.; Xue, X.; Zhuang, Z.; Zheng, J.; Lin, Z., Aggregation-Based Abrupt Crystallization from Amorphous Ag_2S to Ag_2S Nanocrystals. *Chem. Commun.* **2015,** *51* (28), 6141-6144.
72. Liu, H.; Hu, W.; Ye, F.; Ding, Y.; Yang, J., Growth Mechanism of Ag_2S Nanocrystals in a Nonpolar Organic Solvent. *RSC Adv.* **2013,** *3* (2), 616-622.
73. Jiang, P.; Chen, Z., Ligand Effect on the Synthesis of Emission-Tunable Near-Infrared Ag_2S Quantum Dots. *New J. Chem.* **2017,** *41* (13), 5707-5712.
74. Sharma, R. C.; Chang, Y. A., The Ag−S (Silver-Sulfur) system. *Bull. Alloy Phase Diagr.* **1986,** *7* (3), 263-269.
75. Lim, W. P.; Zhang, Z.; Low, H. Y.; Chin, W. S., Preparation of Ag2S Nanocrystals of Predictable Shape and Size. *Angew. Chem. Int. Ed.* **2004,** *43* (42), 5685-5689.
76. Penfield, S. L., ART. XV.--On Canfieldite a new Germanium Mineral and on the Chemical Composition of Argyrodite. *American Journal of Science (1880-1910)* **1893,** *46* (272), 107.
77. Sturm, C.; Boccalon, N.; Ramirez, D.; Kleinke, H., Stability and Thermoelectric Properties of the Canfieldite Ag_8SnS_6. *ACS Appl. Energy Mater.* **2021,** *4* (9), 10244-10251.
78. Liu, Y.; Liu, M.; Swihart, M. T., Plasmonic Copper Sulfide-Based Materials: A Brief Introduction to Their Synthesis, Doping, Alloying, and Applications. *J. Phys. Chem. C* **2017,** *121* (25), 13435-13447.
79. Tan, J. M. R.; Scott, M. C.; Hao, W.; Baikie, T.; Nelson, C. T.; Pedireddy, S.; Tao, R.; Ling, X.; Magdassi, S.; White, T.; Li, S.; Minor, A. M.; Zheng, H.; Wong, L. H., Revealing Cation-Exchange-Induced Phase Transformations in Multielemental Chalcogenide Nanoparticles. *Chem. Mater.* **2017,** *29* (21), 9192-9199.
80. Pietak, K.; Jastrzebski, C.; Zberecki, K.; Jastrzebski, D. J.; Paszkowicz, W.; Podsiadlo, S., Synthesis and Structural Characterization of Ag_2ZnSnS_4 Crystals. *J. Solid State Chem.* **2020,** *290*, 121467.
81. Cheng, A.-J.; Manno, M.; Khare, A.; Leighton, C.; Campbell, S. A.; Aydil, E. S., Imaging and Phase Identification of Cu_2ZnSnS_4 Thin Films Using Confocal Raman Spectroscopy. *J. Vac. Sci. Technol.* **2011,** *29* (5), 051203.
82. Anderson, N. C.; Hendricks, M. P.; Choi, J. J.; Owen, J. S., Ligand Exchange and the Stoichiometry of Metal Chalcogenide Nanocrystals: Spectroscopic Observation of Facile Metal-Carboxylate Displacement and Binding. *Journal of the American Chemical Society* **2013,** *135* (49), 18536-18548.
83. Kameyama, T.; Fujita, S.; Furusawa, H.; Torimoto, T., Size-Controlled Synthesis of Ag8SnS6 Nanocrystals for Efficient Photoenergy Conversion Systems Driven by Visible and Near-IR Lights. *Part. Part. Syst. Charact.* **2014,** *31* (11), 1122-1126.

84. Li, B.; Xie, Y.; Huang, J.; Su, H.; Qian, Y., Synthesis and Characterization of Ternary Chalcogenides Ag_8SnE_6 (E=S, Se). *J. Solid State Chem.* **2000,** *149* (2), 338-340.
85. Ji, X.; Copenhaver, D.; Sichmeller, C.; Peng, X., Ligand Bonding and Dynamics on Colloidal Nanocrystals at Room Temperature: The Case of Alkylamines on CdSe Nanocrystals. *J. Am. Chem. Soc.* **2008,** *130* (17), 5726-5735.
86. Fritzinger, B.; Moreels, I.; Lommens, P.; Koole, R.; Hens, Z.; Martins, J. C., *In Situ* Observation of Rapid Ligand Exchange in Colloidal Nanocrystal Suspensions Using Transfer NOE Nuclear Magnetic Resonance Spectroscopy. *J. Am. Chem. Soc.* **2009,** *131* (8), 3024-3032.
87. Lei, H.; Li, T.; Li, J.; Zhu, J.; Zhang, H.; Qin, H.; Kong, X.; Wang, L.; Peng, X., Reversible Facet Reconstruction of CdSe/CdS Core/Shell Nanocrystals by Facet–Ligand Pairing. *Journal of the American Chemical Society* **2023,** *145* (12), 6798-6810.
88. De Roo, J.; Yazdani, N.; Drijvers, E.; Lauria, A.; Maes, J.; Owen, J. S.; Van Driessche, I.; Niederberger, M.; Wood, V.; Martins, J. C.; Infante, I.; Hens, Z., Probing Solvent–Ligand Interactions in Colloidal Nanocrystals by the NMR Line Broadening. *Chem. Mater.* **2018,** *30* (15), 5485-5492.
89. Kessler, M. L.; Starr, H. E.; Knauf, R. R.; Rountree, K. J.; Dempsey, J. L., Exchange Equilibria of Carboxylate-Terminated Ligands at PbS Nanocrystal Surfaces. *PCCP* **2018,** *20* (36), 23649-23655.
90. Wang, Z.; Wen, X.-D.; Hoffmann, R.; Son, J. S.; Li, R.; Fang, C.-C.; Smilgies, D.-M.; Hyeon, T., Reconstructing a Solid-Solid Phase Transformation Pathway in CdSe Nanosheets with Associated Soft Ligands. *PNAS* **2010,** *107* (40), 17119-17124.
91. Bothner-By, A. A.; Stephens, R. L.; Lee, J.; Warren, C. D.; Jeanloz, R. W., Structure Determination of a Tetrasaccharide: Transient Nuclear Overhauser Effects in the Rotating Frame. *J. Am. Chem. Soc.* **1984,** *106* (3), 811-813.
92. Otting, G., NMR Studies of Water Bound to Biological Molecules. *Prog. Nucl. Magn. Reson. Spectrosc.* **1997,** *31* (2), 259-285.
93. Baranov, D.; Lynch, M. J.; Curtis, A. C.; Carollo, A. R.; Douglass, C. R.; Mateo-Tejada, A. M.; Jonas, D. M., Purification of Oleylamine for Materials Synthesis and Spectroscopic Diagnostics for trans Isomers. *Chem. Mater.* **2019,** *31* (4), 1223-1230.
94. Green, P. B.; Villanueva, F. Y.; Demmans, K. Z.; Imperiale, C. J.; Hasham, M.; Nikbin, E.; Howe, J. Y.; Burns, D. C.; Wilson, M. W. B., PbS Nanocrystals Made Using Excess Lead Chloride Have a Halide-Perovskite-Like Surface. *Chem. Mater.* **2021,** *33* (23), 9270-9284.
95. Fisher, B. R.; Eisler, H.-J.; Stott, N. E.; Bawendi, M. G., Emission Intensity Dependence and Single-Exponential Behavior In Single Colloidal Quantum Dot Fluorescence Lifetimes. *J. Phys. Chem. B* **2004,** *108* (1), 143-148.
96. Fisher, A. A. E.; Osborne, M. A.; Day, I. J.; Lucena Alcalde, G., Measurement of Ligand Coverage on Cadmium Selenide Nanocrystals and its Influence on Dielectric Dependent Photoluminescence Intermittency. *Commun. Chem* **2019,** *2* (1), 63.
97. Lee, Y. J.; Jeon, I. C.; Paik, W.-k.; Kim, K., Self-Assembly of 1,2-Benzenedithiol on Gold and Silver: Fourier Transform Infrared Spectroscopy and Quartz Crystal Microbalance Study. *Langmuir* **1996,** *12* (24), 5830-5837.
98. Rong, H.-T.; Frey, S.; Yang, Y.-J.; Zharnikov, M.; Buck, M.; Wühn, M.; Wöll, C.; Helmchen, G., On the Importance of the Headgroup Substrate Bond in Thiol Monolayers: A Study of Biphenyl-Based Thiols on Gold and Silver. *Langmuir* **2001,** *17* (5), 1582-1593.

99. Zhu, C.-N.; Jiang, P.; Zhang, Z.-L.; Zhu, D.-L.; Tian, Z.-Q.; Pang, D.-W., Ag_2Se Quantum Dots with Tunable Emission in the Second Near-Infrared Window. *ACS Appl. Mater. Interfaces* **2013,** *5* (4), 1186-1189.
100. Yang, L.; Guihen, E.; Glennon, J. D., Alkylthiol Gold Nanoparticles in Sol-Gel-Based Open Tubular Capillary Electrochromatography. *J. Sep. Sci.* **2005,** *28* (8), 757-766.
101. Hines, M. A.; Guyot-Sionnest, P., Synthesis and Characterization of Strongly Luminescing ZnS-Capped CdSe Nanocrystals. *The Journal of Physical Chemistry* **1996,** *100* (2), 468-471.
102. Peng, X.; Schlamp, M. C.; Kadavanich, A. V.; Alivisatos, A. P., Epitaxial Growth of Highly Luminescent CdSe/CdS Core/Shell Nanocrystals with Photostability and Electronic Accessibility. *Journal of the American Chemical Society* **1997,** *119* (30), 7019-7029.
103. De Roo, J.; Huang, Z.; Schuster, N. J.; Hamachi, L. S.; Congreve, D. N.; Xu, Z.; Xia, P.; Fishman, D. A.; Lian, T.; Owen, J. S.; Tang, M. L., Anthracene Diphosphate Ligands for CdSe Quantum Dots; Molecular Design for Efficient Upconversion. *Chem. Mater.* **2020,** *32* (4), 1461-1466.
104. Veselska, O.; Dessal, C.; Melizi, S.; Guillou, N.; Podbevšek, D.; Ledoux, G.; Elkaim, E.; Fateeva, A.; Demessence, A., New Lamellar Silver Thiolate Coordination Polymers with Tunable Photoluminescence Energies by Metal Substitution. *Inorg. Chem.* **2019,** *58* (1), 99-105.
105. Wang, J.; Graf, R.; Riedinger, A., Lamellar Silver Thiolate Coordination Polymers with Reversibly Switchable Blue-to-Near Infrared Optical Transitions. *J. Mater. Chem. C* **2021,** *9* (34), 11079-11084.
106. Knauf, R. R.; Lennox, J. C.; Dempsey, J. L., Quantifying Ligand Exchange Reactions at CdSe Nanocrystal Surfaces. *Chem. Mater.* **2016,** *28* (13), 4762-4770.
107. Pan, Z.; Mora-Seró, I.; Shen, Q.; Zhang, H.; Li, Y.; Zhao, K.; Wang, J.; Zhong, X.; Bisquert, J., High-Efficiency "Green" Quantum Dot Solar Cells. *J. Am. Chem. Soc.* **2014,** *136* (25), 9203-9210.
108. Gromova, M.; Lefrançois, A.; Vaure, L.; Agnese, F.; Aldakov, D.; Maurice, A.; Djurado, D.; Lebrun, C.; de Geyer, A.; Schülli, T. U.; Pouget, S.; Reiss, P., Growth Mechanism and Surface State of $CuInS_2$ Nanocrystals Synthesized with Dodecanethiol. *J. Am. Chem. Soc.* **2017,** *139* (44), 15748-15759.
109. Fan, F.; Voznyy, O.; Sabatini, R. P.; Bicanic, K. T.; Adachi, M. M.; McBride, J. R.; Reid, K. R.; Park, Y.-S.; Li, X.; Jain, A.; Quintero-Bermudez, R.; Saravanapavanantham, M.; Liu, M.; Korkusinski, M.; Hawrylak, P.; Klimov, V. I.; Rosenthal, S. J.; Hoogland, S.; Sargent, E. H., Continuous-Wave Lasing in Colloidal Quantum Dot Solids Enabled by Facet-Selective Epitaxy. *Nature* **2017,** *544* (7648), 75-79.
110. Liu, Z.-Y.; Liu, A.-A.; Fu, H.; Cheng, Q.-Y.; Zhang, M.-Y.; Pan, M.-M.; Liu, L.-P.; Luo, M.-Y.; Tang, B.; Zhao, W.; Kong, J.; Shao, X.; Pang, D.-W., Breaking Through the Size Control Dilemma of Silver Chalcogenide Quantum Dots *Via* Trialkylphosphine-Induced Ripening: Leading to Ag_2Te Emitting from 950 to 2100 nm. *J. Am. Chem. Soc.* **2021,** *143* (32), 12867-12877.
111. Ronchi, A.; Capitani, C.; Pinchetti, V.; Gariano, G.; Zaffalon, M. L.; Meinardi, F.; Brovelli, S.; Monguzzi, A., High Photon Upconversion Efficiency with Hybrid Triplet Sensitizers by Ultrafast Hole-Routing in Electronic-Doped Nanocrystals. *Adv. Mater.* **2020,** *32* (37), 2002953.
112. Dexter, D. L., A Theory of Sensitized Luminescence in Solids. *The Journal of Chemical Physics* **1953,** *21* (5), 836-850.
113. Limberg, D. K.; Kang, J.-H.; Hayward, R. C., Triplet–Triplet Annihilation Photopolymerization for High-Resolution 3D Printing. *J. Am. Chem. Soc.* **2022,** *144* (12), 5226-5232.

114. Murov, S. L.; Carmichael, I.; Hug, G. L., *Handbook of Photochemistry, Second Edition*. Taylor & Francis: 1993.
115. Xia, P.; Raulerson, E. K.; Coleman, D.; Gerke, C. S.; Mangolini, L.; Tang, M. L.; Roberts, S. T., Achieving Spin-Triplet Exciton Transfer Between Silicon and Molecular Acceptors for Photon Upconversion. *Nat. Chem.* **2020,** *12* (2), 137-144.
116. Lai, R.; Sang, Y.; Zhao, Y.; Wu, K., Triplet Sensitization and Photon Upconversion Using InP-Based Quantum Dots. *J. Am. Chem. Soc.* **2020,** *142* (47), 19825-19829.
117. Singh-Rachford, T. N.; Castellano, F. N., Photon Upconversion Based on Sensitized Triplet–Triplet Annihilation. *Coord. Chem. Rev.* **2010,** *254* (21), 2560-2573.
118. Wieghold, S.; Bieber, A. S.; VanOrman, Z. A.; Daley, L.; Leger, M.; Correa-Baena, J.-P.; Nienhaus, L., Triplet Sensitization by Lead Halide Perovskite Thin Films for Efficient Solid-State Photon Upconversion at Subsolar Fluxes. *Matter* **2019,** *1* (3), 705-719.
119. Schindelin, J.; Arganda-Carreras, I.; Frise, E.; Kaynig, V.; Longair, M.; Pietzsch, T.; Preibisch, S.; Rueden, C.; Saalfeld, S.; Schmid, B.; Tinevez, J.-Y.; White, D. J.; Hartenstein, V.; Eliceiri, K.; Tomancak, P.; Cardona, A., Fiji: An Open-Source Platform for Biological-Image Analysis. *Nat. Methods* **2012,** *9* (7), 676-682.
120. Fairley, N. F., V.; Richard-Plouet, M.; Guillot-Deudon, C.; Walton, J.; Smith, E.; Flahaut, D.; Greiner, M.; Biesinger, M.; Tougaard, S.; Morgan, D.; Baltrusaitis, J. , Systematic and Collaborative Approach to Problem Solving Using X-Ray Photoelectron Spectroscopy. *Applied Surface Science Advances* **2021,** *5*, 100112.